

# Temperature and Power Dependent Photothermal Properties of Single-Layer MoS<sub>2</sub>

MICHAEL WATSON

A THESIS IN PARTIAL FULFILLMENT OF THE REQUIREMENTS FOR THE DEGREE OF  
MASTER OF SCIENCE

THE DEPARTMENT OF PHYSICS, ASTRONOMY, AND GEOSCIENCES

TOWSON UNIVERSITY

8000 YORK ROAD

TOWSON, MD 21252

DECEMBER, 2013

TOWSON UNIVERSITY  
OFFICE OF GRADUATE STUDIES

THESIS APPROVAL PAGE

This is to certify that the thesis prepared by \_\_\_\_\_ [INSERT Student's Name]  
Michael Watson

entitled\_ [INSERT Title of Thesis] \_\_\_\_\_  
Temperature and power Dependent Photothermal Properties of Single-layer MoS2

has been approved by the thesis committee as satisfactorily completing the thesis  
requirements for the degree \_ [INSERT Type of Degree] \_\_\_\_\_ Master of Science  
(for example, Master of Science)

Jeff R. Simpson (Jeff Simpson)  
Chair, Thesis Committee

2013 Dec. 18  
Date

Rajeswari KOLAGANI  
Committee Member

12/18/13  
Date

Jiu-An Yan (Jiu-An Yan)  
Committee Member

12/18/13  
Date

\_\_\_\_\_  
Committee Member

\_\_\_\_\_  
Date

\_\_\_\_\_  
Committee Member

\_\_\_\_\_  
Date

Janet V. Dehany  
Dean of Graduate Studies

1/7/14  
Date

## Abstract

The discovery of graphene, nearly a decade ago [1, 2, 3], has since given interest into other atomically thin, two-dimensional(2D) crystals. One such material is mono-layer molybdenum disulphide ( $\text{MoS}_2$ ). Electronic device manufactures in particular have found 2D materials such as  $\text{MoS}_2$  interesting because of the physical and electronic properties.  $\text{MoS}_2$  can be fashioned into electronic components such as field-effect transistors (FETs) or logic gates easily and are particularly thin. This interest means  $\text{MoS}_2$  must be understood from an electronic and physical perspective before it can fully be integrated into electronic devices. To understand  $\text{MoS}_2$  better a comprehensive power and temperature dependent study on  $\text{MoS}_2$  was done using both Raman and photoluminescent spectroscopies. Mechanical ex-foliation of  $\text{MoS}_2$  from bulk provides single-layer flakes, which are then transferred either to sapphire substrates or suspended over holes in  $\text{Si}/\text{Si}_3\text{N}_4$ . We measure temperature dependence from  $\approx 100$  K to 400 K and power dependence from  $\approx 6 \mu\text{W}$  to  $\approx 7$  mW using an Argon laser at 514.5 nm and a HeNe laser at 632.8 nm. Raman spectroscopy was used for initial identification of a single-layer flake of  $\text{MoS}_2$ . In  $\text{MoS}_2$  when the two Raman peaks, the  $A_{1g}$  and  $E_{2g}^1$  are less than  $18 \text{ cm}^{-1}$  the flake is considered single layer.[4] The thermal conductivity of  $\text{MoS}_2$  was experimentally extracted from Raman temperature and power measurements using linear coefficients,  $\chi_T$  and  $\chi_P$ , for temperature and power dependence of the peak position respectively.[5] This value of thermal conductivity  $\kappa$  was calculated to be  $\approx 34.5 \text{ W m}^{-1} \text{ K}^{-1}$ . [5] Temperature and power dependent photoluminescent (PL) spectroscopy was used to explore the band-gap and energy transitions of  $\text{MoS}_2$ . The PL spectrum exhibits a main excitonic

peak(A) at  $\approx 1.87$  eV, which consist of both neutral excitons and charged trions (A- or A+).[4] The photothermal properties of a material are important when a material is going to be used in electronic devices. The materials thermal conductivity is important for proper heat management in a device. This work reports thermal conductivity along with important insight into the band-gap. All of this information about the photothermal reaction of the material is necessary before MoS<sub>2</sub> can be implemented into electronic devices.

# Table of Contents

<b>Abstract</b>	<b>iii</b>
<b>Table of Contents</b>	<b>v</b>
<b>List of Figures</b>	<b>vii</b>
<b>List of Tables</b>	<b>ix</b>
<b>1 Introduction</b>	<b>1</b>
<b>2 Experimental Methods</b>	<b>7</b>
2.1 Instrumentation . . . . .	7
2.2 Raman Spectroscopy Background . . . . .	9
2.3 Photoluminescent Spectroscopy Background . . . . .	14
2.4 Mono-layer MoS <sub>2</sub> Samples . . . . .	18
<b>3 Raman Spectroscopy on Monolayer MoS<sub>2</sub></b>	<b>21</b>
3.1 Temperature Dependence . . . . .	23

3.2	Power Dependence . . . . .	28
3.3	Thermal Conductivity . . . . .	32
<b>4</b>	<b>Photoluminescence of Mono-layer MoS<sub>2</sub></b>	<b>34</b>
4.1	Temperature Dependence of Single-Layer MoS <sub>2</sub> . . . . .	36
4.2	Power Dependence of Single-Layer MoS <sub>2</sub> . . . . .	38
<b>5</b>	<b>Conclusion</b>	<b>48</b>
	<b>Bibliography</b>	<b>51</b>
	<b>Curriculum Vitae</b>	<b>57</b>

# List of Figures

1.1	MoS <sub>2</sub> Crystal Structure . . . . .	2
1.2	Optical Micrograph of a Single-layer MoS <sub>2</sub> device . . . . .	3
1.3	MoS <sub>2</sub> Band Structure . . . . .	4
1.4	Raman and IR Active Modes . . . . .	6
2.1	Schematic of Experimental Micro-Raman and Micro-PL Instrumentation. . . . .	8
2.2	Stokes and Anti-Stokes Raman Scattering Process Diagram . . . . .	10
2.3	Feynman diagram for Raman scattering. . . . .	11
2.4	Energy-level Diagram Illustrating Rayleigh, Stokes, and Anti-Stokes Scattering . . . . .	11
2.5	Spectrum illustrating Stokes and Anti-Stokes with green incident laser	13
2.6	Chemoluminescence Example . . . . .	14
2.7	Conduction and Valence Bands of Direct and Indirect Band-gaps . . . . .	15
2.8	Exciton and Trion Diagrams . . . . .	16
2.9	Energy Level Diagram of Photoluminescence Process. . . . .	17

2.10	Optical Micrograph of Mono-layer MoS <sub>2</sub> With Other Information . . .	19
2.11	Optical Micrograph of Supported MoS <sub>2</sub> . . . . .	20
2.12	Supported MoS <sub>2</sub> on Al <sub>2</sub> O <sub>3</sub> substrate . . . . .	20
3.1	Layer Dependence of $E_{2g}^1$ and $A_{1g}$ Peak Frequencies . . . . .	22
3.2	Raman Spectra . . . . .	24
3.3	The Temperature Dependence of the Scattering Rate . . . . .	28
3.4	Power Depended Raman Spectra . . . . .	30
3.5	Non-Linear Power Dependent Peak Frequencies . . . . .	31
4.1	Temperature Dependent PL of Suspended Sample . . . . .	36
4.2	Temperature Dependent PL Peak Position of Suspended and Supported Samples . . . . .	37
4.3	Non Linear Power Dependence for Supported Sample of PL Peak Intensity . . . . .	39
4.4	Non Linear Power Dependence for Supported Sample of PL Peak Position . . . . .	40
4.5	Non Linear Power Dependence for Supported Sample of PL Peak Width	41
4.6	Spectrum of Supported Sample at .0311 mW Excitation Power . . . . .	42
4.7	Spectrum of Supported Sample .685 mW Excitation Power . . . . .	43
4.8	Linear Power Dependence of PL Peak Height . . . . .	44
4.9	Linear Power Dependence of PL Peak Position . . . . .	45
4.10	Linear Power Dependence of PL Peak Width . . . . .	46

# List of Tables

3.1	First-order temperature coefficients $\chi_T$ , power coefficients $\chi_P$ , and thermal conductivity $\kappa$ obtained from Raman spectra. . . . .	26
3.2	Thermal conductivities . . . . .	33
4.1	Several Band-Gap Energies at Low T and 300 K . . . . .	35
4.2	Table of substrate effects on single-layer MoS <sub>2</sub> . . . . .	47

# Chapter 1

## Introduction

The discovery of graphene[1, 2, 3], nearly a decade ago, began extensive research into atomically thin, two-dimensional (2D) crystals. Two examples of these 2D materials are transition-metal dichalcogenide (TMD) semiconductors[3, 6] and boron-nitride.[6] Graphene shows interesting characteristics such as a large thermal conductivity, low dimensionality, and strain tuned electronic structure.[7] Graphene, however, does not have a naturally occurring band-gap, it is a semi-metal. Compared to graphene, the presence of a band-gap in TMDs is more desirable for electrical device applications, such as a field-effect-transistor (FET). The incorporation of molybdenum disulphide ( $\text{MoS}_2$ ), or other single-layer materials like graphene allow manufacturers to approach a new size of electronics.[8] Recent experimental and theoretical work shows that these layered TMD band-structures undergo a transition from indirect to direct bandgap. This occurs when their layer thickness is reduced from bulk to single-layer, which also leads to a pronounced photoluminescence.[9, 4, 10]

$\text{MoS}_2$  is one of the most stable layered TMDs. The bulk  $\text{MoS}_2$  consists of S-Mo-S layers weakly bonded by van der Waals (vdW) interactions. The crystal structure and unit cell diagram are shown in Figure 1.1 where (a) the atomic structure for

bulk and single layer, (b) the side view of two-layer, and (c) the top view of the MoS<sub>2</sub> crystal structure are seen.[11] Single-layer MoS<sub>2</sub> is a low-dimensional material

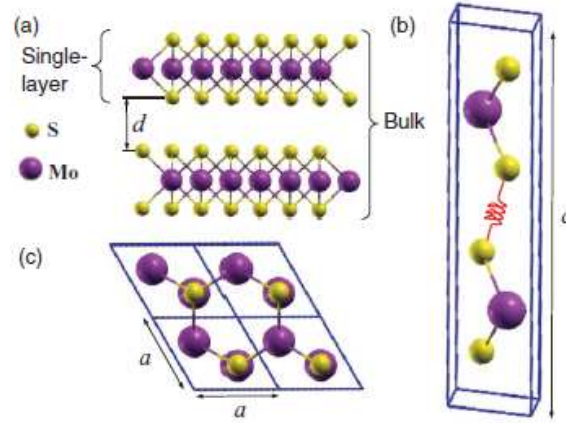


Figure 1.1: This crystal structure of MoS<sub>2</sub> shows (a) bulk and single-layer structure, (b) the side view of a bulk unit cell, and (c) the top view of MoS<sub>2</sub> unit cell. Above the interlayer distance  $d$  and the primitive vectors  $\mathbf{a} = (a, 0, 0)$  and  $\mathbf{c} = (0, 0, c)$  are shown. The van der Waals interaction is shown by the spring.[11]

that also consists of the same S-Mo-S layers as bulk but a single-layer of 2D MoS<sub>2</sub> is three layers of atoms. Currently, MoS<sub>2</sub> is mostly used in bulk as a dry lubricant. Transistors constructed from few-layer and mono-layer MoS<sub>2</sub> show potential for low-power electrical device platforms.[8, 12] Devices, such as the one shown in Figure 1.2, are promising for future low power electronic components. These devices, such as the FET described before, are smaller, created from less expensive materials, and are easily tunable through strain or doping for different band-gaps. Figure 1.2 shows (a) an optical micrograph of a mono-layer MoS<sub>2</sub> flake deposited on top of a SiO<sub>2</sub>/Si substrate, (b) the integrated circuit based on the flake shown in (a) with three Au electrical leads and (c) the cross-sectional representation of a mono-layer

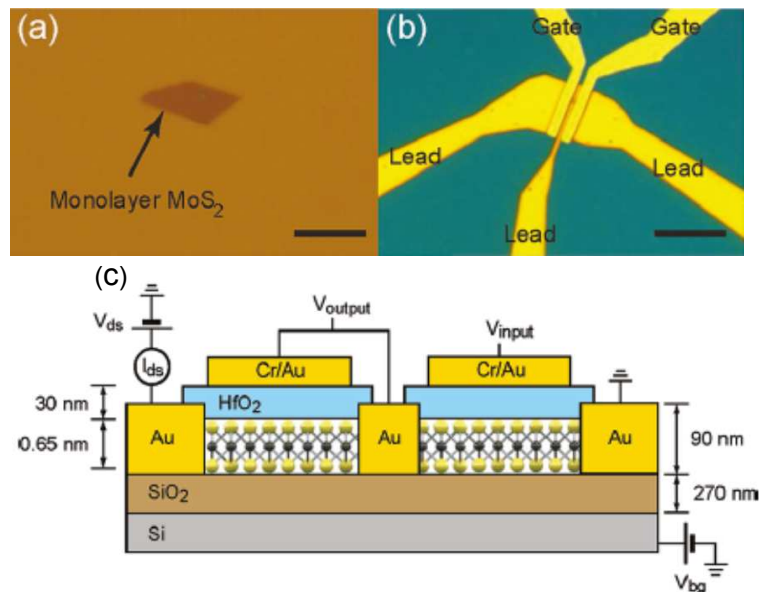


Figure 1.2: (a) An optical micrograph of a mono-layer MoS<sub>2</sub> flake deposited on top of a Si substrate. 10  $\mu\text{m}$  scale bar. (b) An integrated circuit based on the flake shown in (a). There are three Au electrical leads that can act as a source, drain, and output terminals with two local gates. (c) A cross-sectional view of the structure of a mono-layer MoS<sub>2</sub> integrated circuit together with electrical connections used to characterize the device. [8]

MoS<sub>2</sub> integrated circuit.[8]

Graphene has no naturally occurring bandgap making it more difficult to incorporate it easily into electronic devices. A bandgap in graphene can be formed through straining the material, doping the material, or using other mechanisms, but it requires more effort than a naturally occurring bandgap.[13] MoS<sub>2</sub> is a single-layer material that does have a naturally occurring band-gap. The material starts with an indirect gap at 1.2 eV in bulk and then MoS<sub>2</sub> transitions into a direct gap  $\approx 1.9$  eV for mono-layer as shown in figure 1.3. In the band structure figure, photon transitions

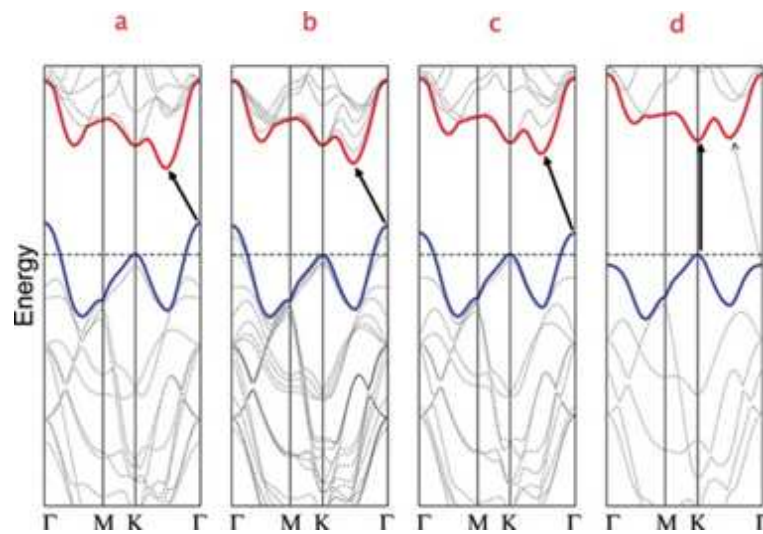


Figure 1.3: The band structure evolves through layer thinning from (a) bulk, (b) quadlayer, (c) bilayer, to (d) monolayer. The blue curves represent the conduction band while the red curves represent the valence bands. The black arrow is the lowest energy transition.[9]

are vertical due to the momentum,  $\hbar k_{ph}$ , of the photon being much less than the  $\hbar k_{BZ}$  of the Brillouin zone where  $k_{ph} = 2\pi/\lambda$  and  $k_{BZ} = 2\pi/a$  where  $\lambda$  is the wavelength of visible light and  $a$  is the lattice constant. In figure 1.3 the conduction band is in red while the valence band is shown in blue. The band structure shows the evolution from bulk to mono-layer for (a) bulk band structure, (b) quad-layer, (c) bilayer, and (d) mono-layer.[9] The K-point transition is seen from an indirect gap in bulk (a) to a direct gap in mono-layer in (d), where the solid arrows represent the lowest energy transition. The transition from an indirect band-gap to a direct band-gap increases the photoluminescent (PL) efficiency.[9] The PL radiative recombinations occurs at the lowest energy possible. The transitions for the band-gap are dictated by conservation of energy and momentum allowing for the main PL recombination to be more intense than other transitions. Along with intensity the transitions are also sensitive to circular polarization, which allows possible device innovation based on input polarization.[14]

MoS<sub>2</sub> has extensive device applications, which give rise to the necessity of research to understand intrinsic characteristics of the material. One physical property that is important for materials in electrical devices is the thermal conductivity,  $\kappa$ . Graphene has superior thermal conductivity at  $\approx 5300 \text{ W m}^{-1} \text{ K}^{-1}$ , which is much higher than MoS<sub>2</sub>. [15] Raman spectroscopy probes lattice interactions and electron-phonon coupling. Figure 1.4 shows where the IR active cannot be Raman active for crystals without inversion symmetry. This figure represents the atomic displacements of the four Raman active modes and one IR active mode ( $E_{1u}$ ) in the unit cell of the bulk MoS<sub>2</sub> crystal as viewed along the [100] direction. Probing the temperature

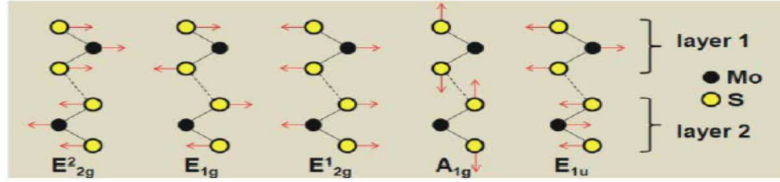


Figure 1.4: Atomic displacements of the four Raman active modes and one IR active mode ( $E_{1u}$ ) in the unit cell of the bulk  $\text{MoS}_2$  crystal as viewed along the  $[100]$  direction.[16]

and power dependence of these Raman modes allows the photothermal properties to be examined. The photothermal properties are the relationships between excitation from photons and thermal energy in the material. This photothermal probing allows the value for  $\kappa$  to be extracted. Raman and photoluminescent spectroscopy give understanding into material layering lattice structure and material constants. This understanding must exist before  $\text{MoS}_2$  can make the jump into current applications.

The background behind the spectroscopic methods that were used will be discussed in chapter 2.4 along with instrumentation and experimental equipment. Then the Raman spectra will be discussed in chapter 3.3, giving insight into how the thermal conductivity was experimentally measured and how the value compares to other materials. Then in chapter 4.2 the PL spectra will be shown and the band-gap of  $\text{MoS}_2$  will be discussed. This band-gap is important to electronic devices and will be compared to other materials of interest. Then finally chapter 5 will discuss overall topics and summarize the previously discussed data.

# Chapter 2

## Experimental Methods

Optical techniques for probing novel condensed matter and nano-scale materials are extremely valuable. Spectroscopic methods provide non-destructive and non-contact options to experimentalists for understanding the fundamental physics of a material. It is possible through Raman spectroscopy to find the number of layers for few and single-layered atomic materials, test electron-phonon interactions, measure photothermal properties of a material, including thermal conductivity  $\kappa$ . Photoluminescent (PL) spectroscopy also allows a non-destructive and contact method for understanding a material's band structure along with defects in the atomic structure.

### 2.1 Instrumentation

The basic experimental set-up for both Raman and PL studies consists of a Renishaw InVia micro-Raman spectrometer employing several excitation lasers, including a Helium-Neon (HeNe) laser with wavelength of 632 nm, a diode with wavelength of 785 nm, and an Argon Ion with wavelength of 514.5 nm. A long-working distance 50X objective lens (numerical aperture  $NA = 0.55$ ) provides a diffraction-

limited spot of  $1.22/\text{NA} \approx 1.14 \mu\text{m}$  and the Gaussian beam width is estimated to be  $2\lambda/(\pi \text{NA}) \approx 0.6 \mu\text{m}$ .<sup>[17]</sup> The samples were mounted in a cryostat cooled by liquid nitrogen. Throughout all of the temperature-dependent measurements, the laser intensity was maintained to be less than approximately  $0.14 \text{ mW}/\text{area}$  to limit local heating by excitation laser. A schematic of the experimental set-up is shown in Figure 2.1. In this micro-Raman spectrometer an excitation laser is focused through a

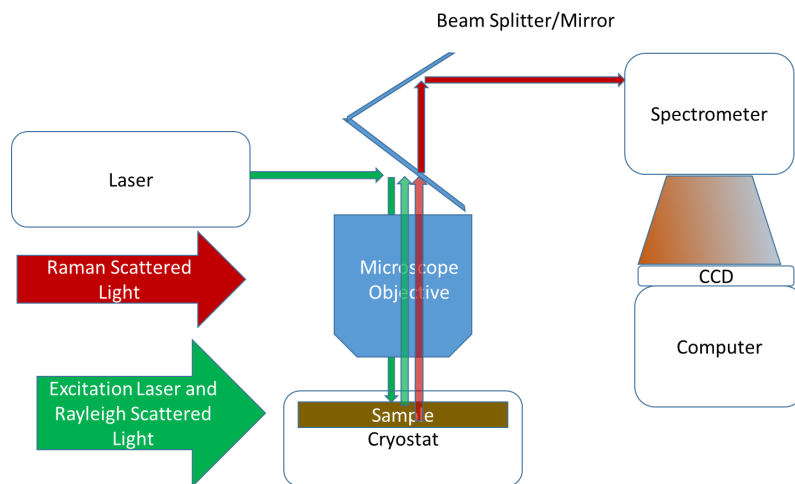


Figure 2.1: Schematic of Experimental Micro-Raman and Micro-PL Instrumentation.

microscope objective. After focusing, the excitation laser reaches the sample, which is in a cryostat for temperature-dependent studies. Then the scattered light ( $180^\circ$  backscattering) from the sample is re-collimated through the microscope objective, directed through a filter to block the Rayleigh scattering, and finally into a grating spectrometer. The spectrometer disperses the light using a grating and directs the scattered and dispersed light to a charge-coupled device (CCD) for spectrum count readings. The Renishaw InVia spectrometer with a Leica microscope attached was

used to perform the measurements in both Raman and PL. The software allows for options, *e.g.*, exposure time and energy range for spectra.

## 2.2 Raman Spectroscopy Background

Raman scattering, unlike Rayleigh scattering where the excitation and the scattered radiation are of the same energy, is an inelastic process. This means in Raman scattering the scattered radiation is of a different energy than the excitation radiation. Raman scattering probes fundamental physical properties of a material, *e.g.* lattice structure, electron-phonon coupling, and defects; Raman is sensitive to lattice vibrations, or phonons, and hence useful to probe the crystal lattice. Raman scattering is related to the dipole moment and the Raman tensor

$$I \propto |e_i \cdot R_{lm}^k Q_k \cdot e_s|^2 \quad (2.1)$$

where the scattering intensity  $I$  is proportional to the square of the Raman tensor  $R_{lm}$  times the magnitude of incident dipole matrix element  $e_i$  times the scattered dipole matrix element  $e_s$ . The Raman tensor is given by

$$R_{lm}(-\omega_i, \omega_s, \omega_q) = \frac{\partial \chi_{lm}(\omega_i)}{\partial Q_k} \cdot \hat{Q}_k(\omega_q) \quad (2.2)$$

where an incident photon polarization is subscripted with  $l$ , the scattered photon polarization is subscripted with  $m$ , incident frequency is  $\omega_i$ , scattered frequency is  $\omega_s$ , phonon frequency is  $\omega_q$ , the lattice coordinate is  $Q$ , and the susceptibility is  $\chi$ .

Raman scattering will either have a higher or lower scattered frequency than the excitation frequency. When the scattered light is of a lower energy it is called Stokes scattering and when it is higher it is called anti-Stokes. The scattered light for both processes are described by:

$$\text{Stokes: } \vec{k}_s = \vec{k}_i - \vec{q}, \quad \omega_s = \omega_i - \omega_q. \quad (2.3)$$

$$\text{anti-Stokes: } \vec{k}_s = \vec{k}_i + \vec{q}, \quad \omega_s = \omega_i + \omega_q. \quad (2.4)$$

This scattering event is represented schematically in figure 2.2. A (a) generic Raman scattering of a photon with specific diagram for (b)emission or absorption(c) of a phonon.[18] is described in equation 2.3 and 2.4 through the wave vector  $\vec{k}$  and

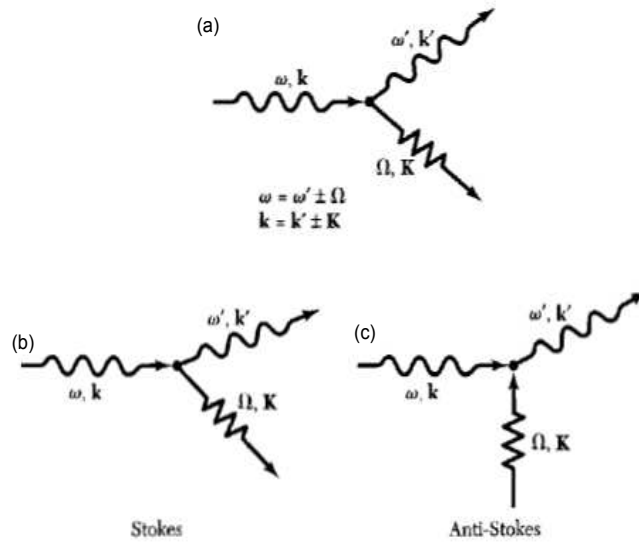


Figure 2.2: (a)Generic Raman scattering of a photon with specific diagram for (b)emission or absorption(c) of a phonon.[18]

frequency  $\omega_i$ . In the equations  $\vec{k}_i$  and  $\omega_i$  represent the incident photon,  $\vec{k}_s$  and  $\omega_s$  represent the scattered photon and  $\vec{K}$  and  $q$  represent the phonon. These equations developed from conservation of energy  $\hbar\omega$  and momentum  $\hbar\vec{k}$ . The Raman scattering event in figure 2.3, is shown by the Feynman diagram. In the Feynman diagram, (1)

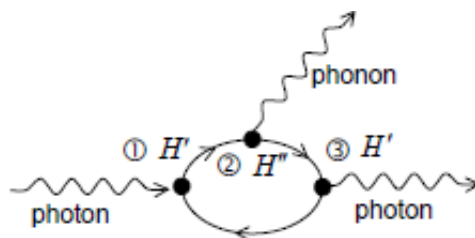


Figure 2.3: Feynman diagram for Raman scattering.

an incident photon is shown (2) interacting with the material. The lattice either gives energy or takes energy from the excited state, after which a photon is re-emitted (3) at a different energy. The energy-level diagram also shows the differences between Stokes, anti-Stokes, and Rayleigh scattering in figure 2.4. This energy is described

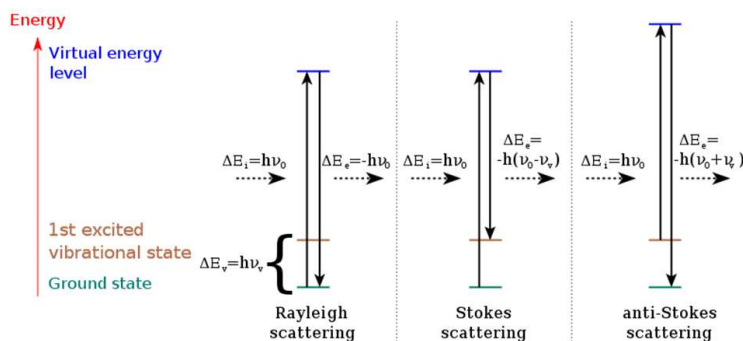


Figure 2.4: Energy-level Diagram Illustrating Rayleigh, Stokes, and Anti-Stokes Scattering

by the Hamiltonian,  $H_{dipole-dipole}(H')$ .  $H'$  is the Hamiltonian of the electric dipole interactions and lattice interaction. This interaction is a third-order, non-linear effect, which means that the materials susceptibility,  $\chi$ , is dependent upon the intensity and frequency of the applied electromagnetic field. This interaction involves an incident photon hitting a material, then the energized electron interacts with phonons in the lattice, and then a photon is emitted(scattered). An incident electromagnetic wave that interacts with a material will induce a local polarization, which will be related to the electromagnetic field  $\vec{E}$ . This interaction is described above through classical mechanics but more accurately described in quantum mechanics with the Hamiltonian described before,  $H'$ :

$$\begin{aligned}
 \text{Step 1 } & \langle \alpha | H' | i \rangle \text{ Incoming Dipole} \\
 \text{Step 2 } & \langle \beta | H'' | \alpha \rangle \text{ electron-phonon Hamiltonian} \\
 \text{Step 3 } & \langle s | H' | \beta \rangle \text{ Outgoing Dipole}
 \end{aligned} \tag{2.5}$$

The Hamiltonians in equation 2.5 are described by their initial states  $|i\rangle$ , interaction intermediate states  $|\alpha\rangle$  and  $|\beta\rangle$  along with the scattered state  $|s\rangle$  where the intermediate states are lattice interactions which are the Hamiltonian of the phonon interactions. The steps described in the equation relate to the steps in figure 2.3.

Figure 2.5 shows a typical Raman spectrum plotting intensity as a function of energy shift. The excitation laser is shown in green, the Stokes shift in red, and the anti-Stokes shift in blue. In anti-Stokes the final momentum and final frequency is described by equation 2.4 and shown in figure 2.2. This Raman scattering event is

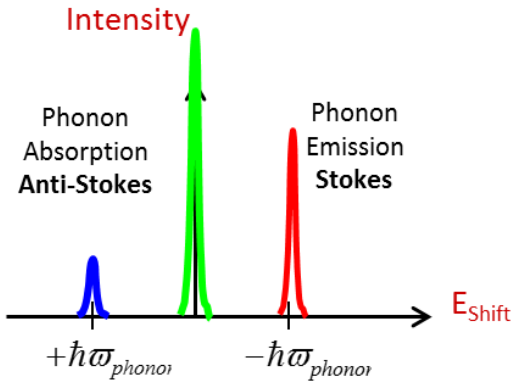


Figure 2.5: This is a representation of a Raman spectrum showing intensity as a function of photon energy shift. The Rayleigh scattering in green is several orders of magnitude greater intensity than the stokes in red and anti-stokes in blue

much less intense than Rayleigh scattering, as shown in figure 2.5. The figure shows how the incident laser's intensity (not to scale) is several orders of magnitude larger than the Raman scattering so it must be filtered out.

One of the useful pieces of information that can be extracted from Raman scattering is the phonon activity in the lattice. Phonons are quasi-particles representing lattice vibrations. These phonons will travel, like a particles, through the lattice structure, either taking energy from the lattice or donating energy. This is where the inelastic scattering originates from for Raman scattering. The photon from the excitation will hit the material in question, after the collision the photon is absorbed. Once it is absorbed that electron configuration may change and result in spontaneous emission.

## 2.3 Photoluminescent Spectroscopy Background

Luminescence is the stimulated emission of light from a material, or radiative recombination of electron-hole pairs. There are several forms of luminescence including electroluminescence stimulated through an electric current, or chemoluminescence which is stimulated by a chemical reaction as seen in figure 2.6, or piezoluminescence which is stimulation from pressure or physical strain. One specific form of lumines-

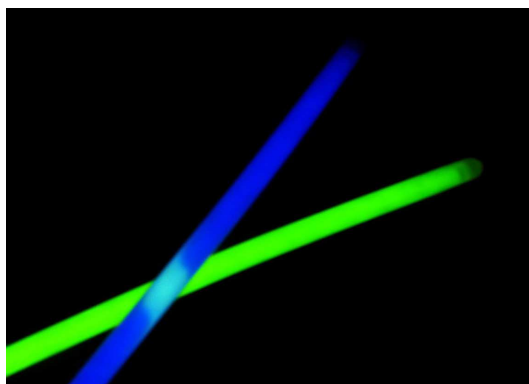


Figure 2.6: An example of chemoluminescence-glow sticks.[D.Muelheim,wikipedia.com;2006]

cence is photoluminescence (PL), which is an excitation as a result of a photon. This excitation of the electron is from the valence band to a higher energy level as seen in figure 2.7 where there is a representation of both (a) a direct band-gap transition and (b) an indirect band-gap transition where there is a momentum change. These electron-hole pairs, or excitons, can be neutral or charge excitons. A neutral exciton is seen in figure 2.8 (a) as a single electron-hole pair. There are also charged excitons called trions, these can also be seen in figure 2.8. These trions either have

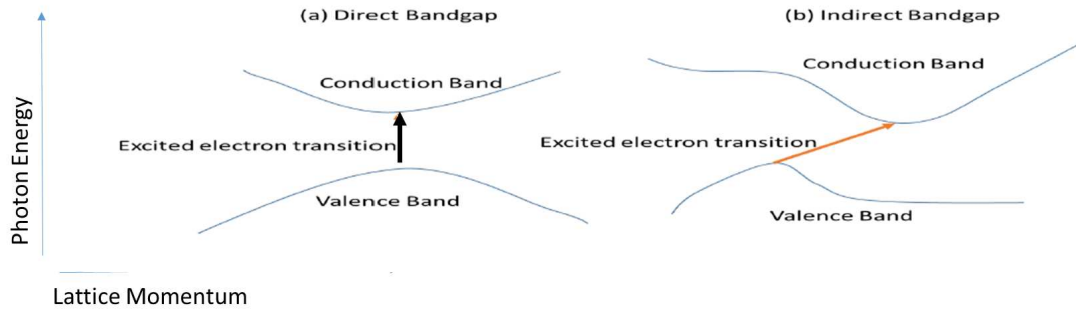


Figure 2.7: This shows the transitions for (a) a direct bandgap transition where vertical line where as (b) which is an indirect bandgap transition is diagonal representing a momentum change.

2.8 (b) two electrons and one hole making them a negative trion or 2.8 (c) two holes and an electron making them a positive trion. These excitons will relax from their excited state through one or more non-radiative processes, such as lattice heating, losing energy before the electrons and holes recombine in a radiative recombination. This process is represented in figure 2.9. We can see in this figure the energy level diagram of a luminescent process from excitation to non-radiative relaxation and on to radiative recombination and photon emission.

Photoluminescent spectroscopy is a useful method for probing electronic structure of materials. It is a non-destructive and non-contact method that has the ability to probe the bandgap energy, impurities and defects in the material such as the lattice defects, and recombination methods along with energy level transitions. Luminescence is a result of a several step process that can be simplified to the luminescence equation 2.6

$$L(\omega) = \frac{\partial}{\partial t} \langle \hat{B}_\omega^\dagger \hat{B}_\omega \rangle \quad , \quad (2.6)$$

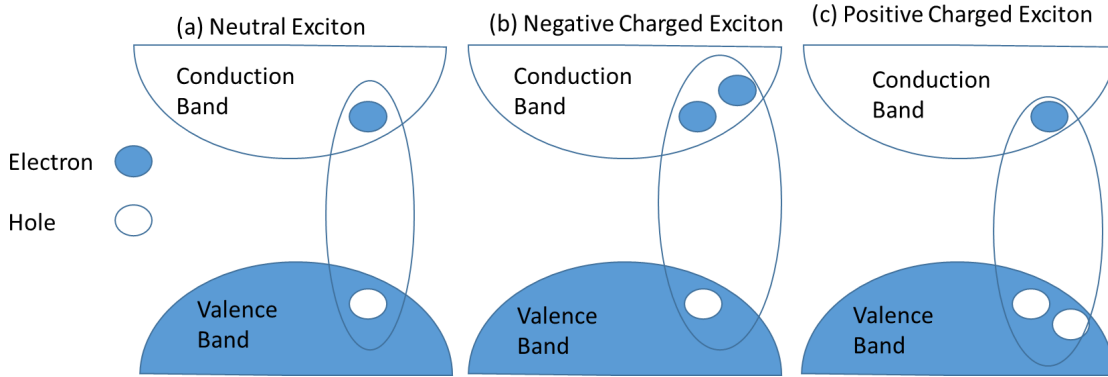


Figure 2.8: Here is a representation of different excitation possibilities. The first is (a) a neutral exciton or electron hole pair, then (b) a negative trion or two electrons and one hole, and (c) a positive trion or one electron and two holes

where  $L(\omega)$ , or the frequency dependent luminescence is equal to the partial time derivative of the expectation value between  $\hat{B}_\omega^\dagger$ , the Boson creation operator and  $\hat{B}_\omega$ , the Boson annihilation operator. Equation 2.6 is a condensed version of a family of equations called the Semiconductor Luminescence Equations.[19] Luminescence, as described previously, is the radiative recombination of an electron-hole pair. The electron-hole pairs must be created and annihilated for the luminescent process to continue. There is non-radiative energy loss in which the electron relaxes from higher energy levels until it reaches the band-gap edge of the conduction band. The electron will then radiatively recombine with a hole in the valence band. Luminescence, then, is a net rate of change between the conduction to the valence band described by  $\frac{dn}{dt}$  where  $n$  is the number of electrons.

$$\frac{dn}{dt} = \alpha_r n_0 p_0 - \alpha_r n(t) p(t) \quad (2.7)$$

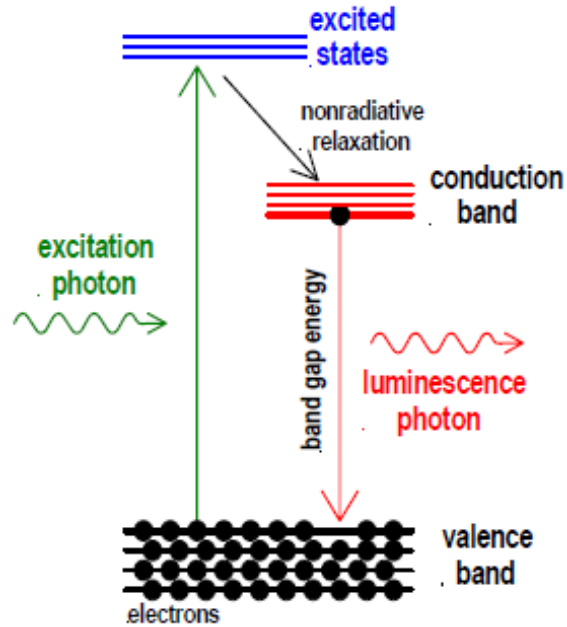


Figure 2.9: Energy Level Diagram of Photoluminescence Process.

where  $\alpha_r$  represents the recombination coefficient,  $p_0$  and  $n_0$  are the initial or stable values for the holes and electrons and the number recombining is subtracted off giving us a total recombination rate over time. Applying equilibrium to the equation can reach a statement for the equilibrium electron change over time

$$\delta n(t) = \Delta n e^{-\frac{t}{\tau_n}} \quad . \quad (2.8)$$

In equation 2.8 the equilibrium state for electrons between the valence and conduction band  $\delta n(t)$  is equal to the change in electrons multiplied by an exponentially decaying ratio of time  $t$  and the lifetime  $\tau_n$  of an electron in the conduction band. The electrons radiatively combining  $n(t)$  is related to the luminescence by a time derivative, in

equation 2.9

$$L(\omega) \propto \frac{\partial \delta n(t)}{\partial t} . \quad (2.9)$$

This proportionality relates the boson annihilation and creation operators to a more understood value of an electron losing energy and radiatively recombining with a hole counterpart in the valence band as shown in equation 2.9.

## 2.4 Mono-layer MoS<sub>2</sub> Samples

There were three separate samples studied in this work: (1) a mono-layer MoS<sub>2</sub> sample suspended on a Si<sub>3</sub>N<sub>4</sub>/SiO<sub>2</sub>/Si substrate,(2) mechanically exfoliated flakes transferred an Al<sub>2</sub>O<sub>3</sub> (sapphire) substrate, (3) mechanically exfoliated flakes on sapphire and covered with a layer of hafnia (HfO<sub>2</sub>). The suspended sample on the Si<sub>3</sub>N<sub>4</sub>/SiO<sub>2</sub>/Si substrate is shown in figure 2.10. To prepare the sample flakes of MoS<sub>2</sub> were first deposited onto SiO<sub>2</sub>/Si wafers using mechanical exfoliation.[1] After the identification of the layer number using optical microscopy[20] and atomic force microscope (AFM), the flakes were transferred onto previously patterned Si<sub>3</sub>N<sub>4</sub>/SiO<sub>2</sub>/Si substrate. The cross-section of the Si<sub>3</sub>N<sub>4</sub>/SiO<sub>2</sub>/Si substrate structure is shown in figure 2.10, where holes with a diameter of 1.2 μm are defined by e-beam lithography and patterned by an etching process on Si<sub>3</sub>N<sub>4</sub>. The suspended mono-layer MoS<sub>2</sub> flake covers the entire region of several holes in the Si<sub>3</sub>N<sub>4</sub>. The height profile measured by AFM at the edge of the flake before the transfer process, as shown in figure 2.10(b), shows a thickness of ≈ 0.8 nm, confirming that the region of interest is mono-layer MoS<sub>2</sub>. The two other samples, as shown in figure 2.11, were prepared by transferring

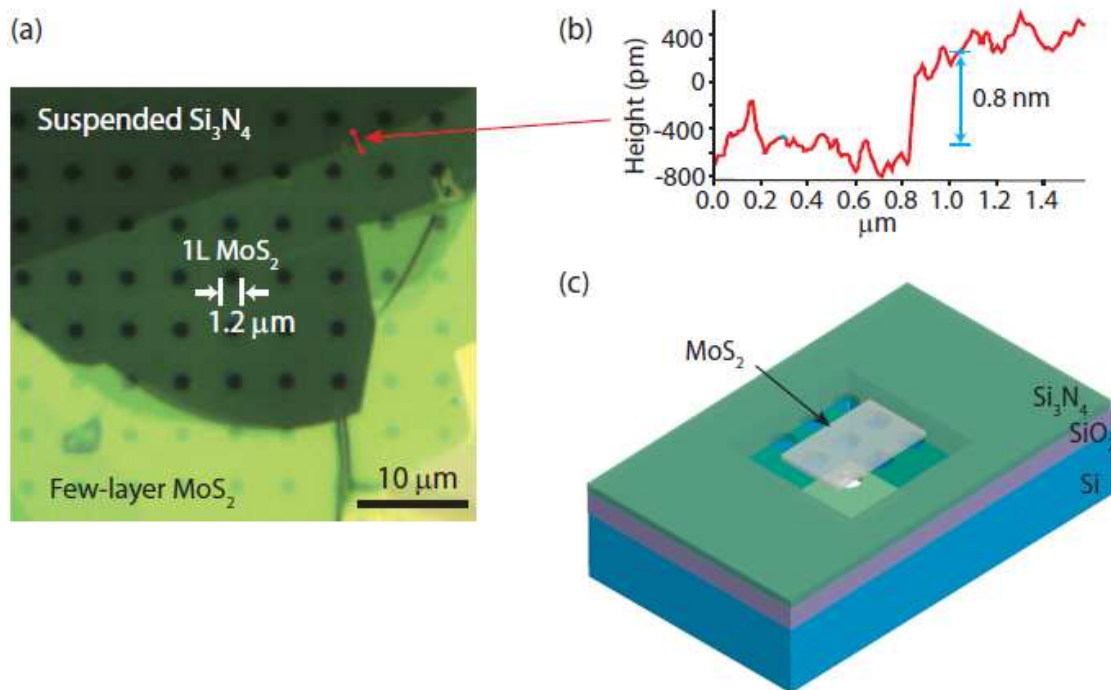


Figure 2.10: MoS<sub>2</sub> suspended on a Si<sub>3</sub>N<sub>4</sub>/SiO<sub>2</sub>/Si substrate. (a) Optical micrograph of flake, (b) AFM step height across the edge of mono-layer flake, (c) Representation of suspended sample.

the mechanically exfoliated flakes to an Al<sub>2</sub>O<sub>3</sub> (sapphire) substrate. After transferring the flake to sapphire one sample was covered with a layer of hafnia (HfO<sub>2</sub>). A representation of both a supported sample with and without the HfO<sub>2</sub> overcoat is shown in figure 2.12.

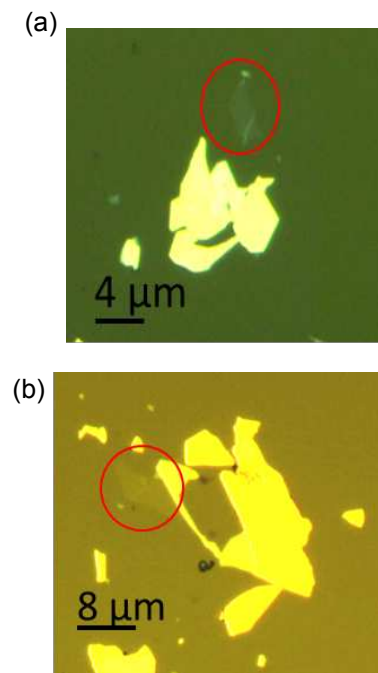


Figure 2.11:  $\text{MoS}_2$  supported on an  $\text{Al}_2\text{O}_3$  substrate (a) with out  $\text{HfO}_2$  overcoat and (b) with  $\text{HfO}_2$  overcoat.

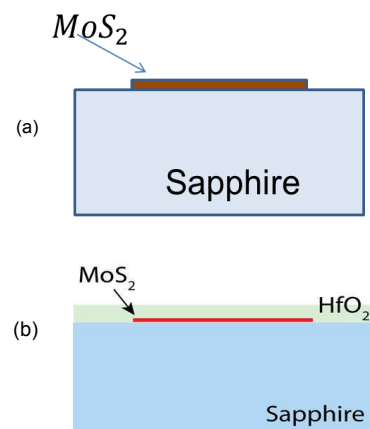


Figure 2.12: Where (a) is without overcoat and (b) is with  $\text{HfO}_2$  overcoat.

## Chapter 3

# Raman Spectroscopy on Monolayer MoS<sub>2</sub>

Raman spectroscopy is sensitive to small changes in phonon frequency, which is useful, considering the presence of interlayer vdW forces affects not only the band structure,[21, 22] but also the lattice vibrations.[16] As a result, Raman spectroscopy is used to determine the layer number of graphene,[23] WS<sub>2</sub>,[24] and MoS<sub>2</sub>[16]. Two prominent peaks, the in-plane  $E_{2g}^1$  and the out-of-plane  $A_{1g}$  modes, are observed in the Raman spectrum of MoS<sub>2</sub>. The phonon frequency difference between the two modes is commonly used as the thickness indicator.[16] Figure 3.1 shows the layer dependency of MoS<sub>2</sub>. It has also been shown that Raman spectral features characterize doping, the dielectric environment, and strain effects of atomically thin MoS<sub>2</sub> flakes by monitoring the change of peak position and full width at half maximum (FWHM) of Raman-active phonons.[25, 26, 27, 28] A detailed temperature and power dependent Raman study was done on mono-layer MoS<sub>2</sub>. To isolate the substrate effects, Raman measurements are included from both suspended and supported mono-layer MoS<sub>2</sub> flakes. Such studies are of fundamental importance for a

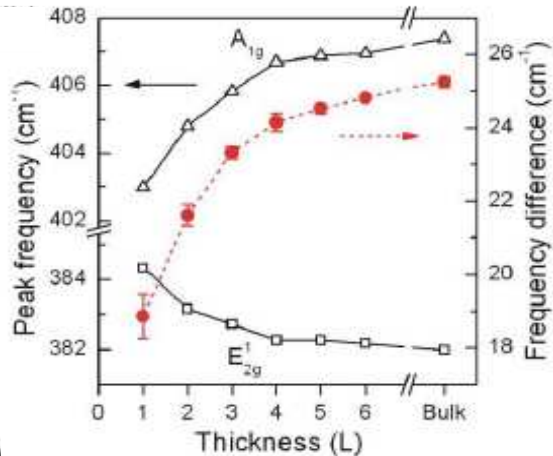


Figure 3.1: The layer dependent frequencies for the  $E_{2g}^1$  and  $A_{1g}$  modes are shown. The  $E_{2g}^1$  (squares) and  $A_{1g}$  (triangles) peak frequencies shift towards each other as layers are removed from bulk to mono-layer. [16] The peak frequencies are shown on the left axis and the peak difference is shown in the right axis.

comprehensive understanding of anharmonic lattice vibrations, thermal expansion, and thermal conductivity.[29, 30, 31, 32, 33] Raman spectroscopy provides a powerful, non-contact method to monitor the local temperature rise induced by light, electrical currents, etc. The combination of both temperature and power dependence of optical phonon frequencies permits extraction of the thermal conductivity  $\kappa$ . [15, 34] Raman spectroscopy has become a major benchmark in determining the number of layers in these few-layered and mono-layered materials like graphene. In graphene the shape of the G' peak help determine if the material in question is truly single-layer. Because the energies involved in lattice vibrations vary drastically in MoS<sub>2</sub> the peak position between the  $E_{2g}^1$  and  $A_{1g}$  peak becomes the main indicator of layer numbers. As the MoS<sub>2</sub> approaches single layer the  $E_{2g}^1$  peak position

shifts to a higher energy while the  $A_{1g}$  peak position shows the opposite. The frequency difference between the two peaks decreases as the layer number decreases from bulk to single-layer. This provides direct insight into layer number through a non-destructive experimental technique. When the peak position difference, or the frequency difference, reaches  $(19 \pm 1) \text{ cm}^{-1}$ ,  $\text{MoS}_2$  is confirmed to be mono-layer.[34] This is shown in figure 3.1 where  $E_{2g}^1$  peak frequencies are shown in squares,  $A_{1g}$  in triangles, and the peak difference is shown in red circles and the right axis is used for the peak differences.

### 3.1 Temperature Dependence

The  $E_{2g}^1$  and  $A_{1g}$  peak positions shift to lower energies as temperature increases. These peak position of the  $E_{2g}^1$  and  $A_{1g}$  were then extracted by fitting two Lorentzian curves to the spectra shown in equation 3.1

$$L(\omega) = \sum_i A_i \frac{\gamma_i^2}{(\omega - \omega_{0i})^2 + \gamma_i^2} \quad , \quad (3.1)$$

where  $A$  represents the amplitude of a peak,  $\gamma$  represents the half width half maximum of the peak, and  $x_0$  represents the peak position and all are indexed with  $i$  for multiple peaks. The temperature-dependent spectra was taken in the experimental apparatus as discussed in the previous section. Figure 3.2 shows four example Raman spectra and their corresponding Lorentzian fits collected from suspended, mono-layer  $\text{MoS}_2$  while the sample temperature ranges from 100 K to 320 K. As seen in the figure, two prominent peaks around  $385 \text{ cm}^{-1}$  and  $405 \text{ cm}^{-1}$  are observed, which correspond

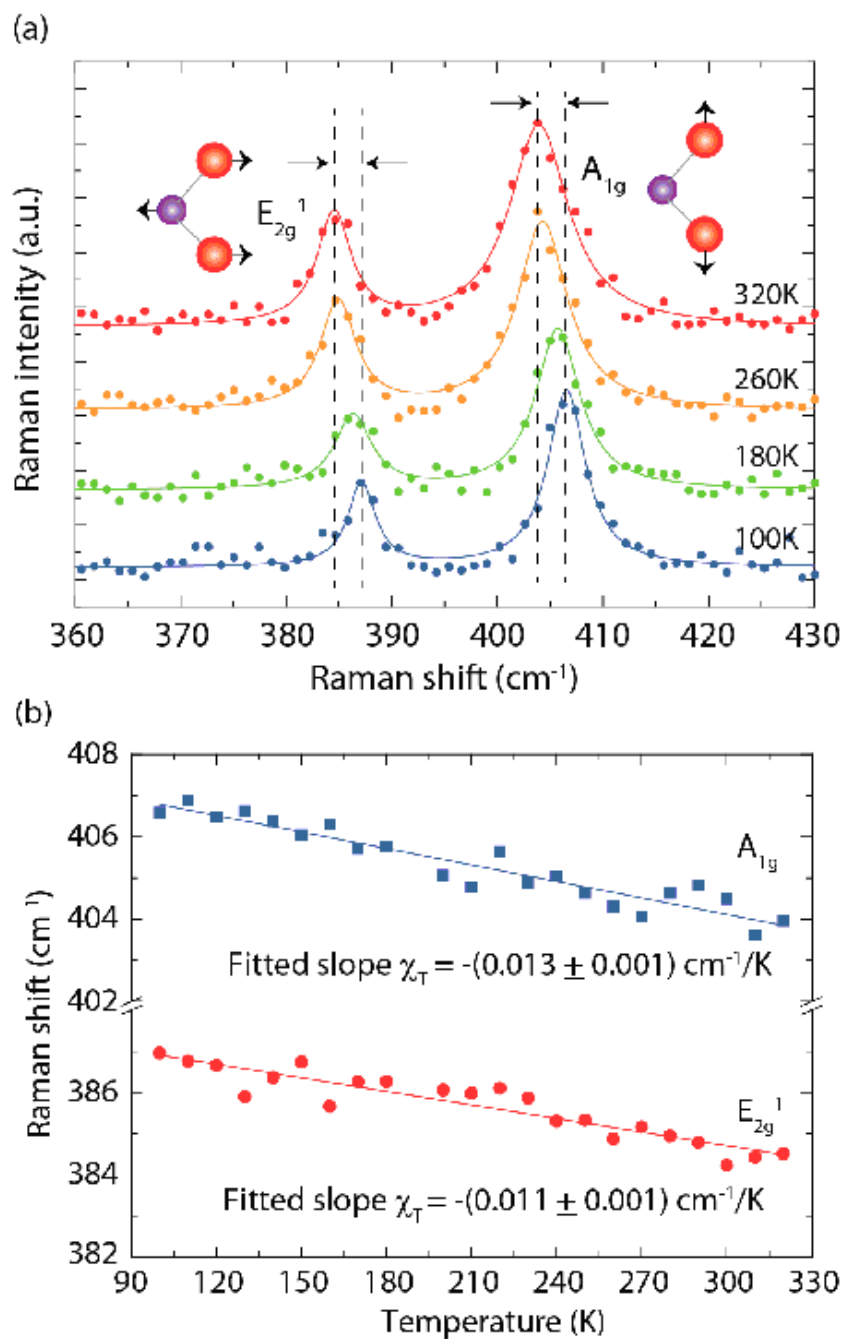


Figure 3.2: (a) Four example Raman spectra of suspended, single-layer,  $\text{MoS}_2$  collected at 100 K, 180 K, 260 K, and 320 K. The vertical offset is for display clarity. (b) Raman peak positions for both  $A_{1g}$  (blue squares) and  $E_{2g}^1$  (red circles) modes as a function of temperature. Fit lines and linear coefficients for temperature dependence,  $\chi_T$ , are shown.

to the in-plane  $E_{2g}^1$  mode and the out-of-plane  $A_{1g}$  mode, respectively.[16] Vibration of the  $E_{2g}^1$  mode involves in-plane opposing motions of sulfur (S) and molybdenum (Mo) atoms and that of the  $A_{1g}$  mode is out-of-plane relative motions of S atoms, as depicted in the insets of figure 3.2(a). As the temperature increases, both of the Raman-active modes soften linearly and the  $A_{1g}$  peak clearly broadens. The  $E_{2g}^1$  mode also broadens, however, it does not broaden at as steep a rate, it is less changed by temperature. Figure 3.2 shows the temperature dependence of the Lorentzian-fit (see equation 3.1). The shift of the peak frequencies from 100 K to 320 K for the  $A_{1g}$  (blue squares) and  $E_{2g}^1$  (red circles) phonons is shown. The evolution of the Raman peak position  $\omega$  as a function of lattice temperature follows a linear dependence

$$\Delta\omega = \omega(T_2) - \omega(T_1) = \chi_T (T_2 - T_1) = \chi_T \Delta T \quad (3.2)$$

where  $\chi_T$ , the slope of temperature dependence, is the first-order temperature coefficient for the respective modes, and  $T$  is the absolute temperature. Non-linear coefficients are not considered here given that they can only be observed at higher temperatures,[15, 34] however, a non-linear dependence was observed in our laser power measurements at room temperature (RT), which will be discussed later. In figure 3.2 four example Raman spectra of suspended, single-layer, MoS<sub>2</sub> collected at 100 K, 180 K, 260 K, and 320 K are shown (a). The vertical offset is for display clarity. In (b) Raman peak positions for both  $A_{1g}$  (blue squares) and  $E_{2g}^1$  (red circles) modes as a function of temperature. Fit lines and linear coefficients for temperature dependence,  $\chi_T$ , are shown. The extracted linear temperature coefficients  $\chi_T$  deter-

mined from the slopes are  $-(0.011 \pm 0.001) \text{ cm}^{-1}/\text{K}$  and  $-(0.013 \pm 0.001) \text{ cm}^{-1}/\text{K}$  for the  $E_{2g}^1$  and  $A_{1g}$  modes, respectively. These values are included in table 3.1

Material	Type	Mode	$\chi_T$ $\left(\frac{\text{cm}^{-1}}{\text{K}}\right)$	$\chi_P$ $\left(\frac{\text{cm}^{-1}}{\text{mW}}\right)$	$\kappa$ $\left(\frac{\text{W}}{\text{mK}}\right)$
<b>MoS<sub>2</sub> monolayer</b>	<b>suspended</b>	<b><math>E_{2g}^1</math> <math>A_{1g}</math></b>	<b>-0.011 -0.013</b>	<b>-12.8 -10.9</b>	<b><math>34.5 \pm 4</math></b>
MoS <sub>2</sub> few-layer	suspended	$E_{2g}^1$ $A_{1g}$	-0.013 <sup>a</sup> -0.012 <sup>a</sup>	-5.4 <sup>a</sup>	52 <sup>a</sup>
<b>MoS<sub>2</sub> monolayer</b>	<b>supported</b>	<b><math>E_{2g}^1</math> <math>A_{1g}</math></b>	<b>-0.017 -0.013</b>	<b>-2.2<sup>b</sup> -0.09<sup>b</sup></b>	<b>223</b>
graphene mono-layer	suspended	G		-1.2 <sup>c</sup>	5300 $\pm 480^c$
graphene mono-layer	supported	G	-0.016 <sup>d</sup>		
graphene bilayer	supported	G	-0.015 <sup>e</sup>		
HOPG		G	-0.011 <sup>f</sup>		

**Bold entries** represents this work and Ref [5]. <sup>a</sup> Ref. [34]  
<sup>b</sup> Ref. [25]    <sup>c</sup> Ref. [15]    <sup>d</sup> Ref. [33]    <sup>e</sup> Ref. [10]    <sup>f</sup> Ref. [35]

Table 3.1: First-order temperature coefficients  $\chi_T$ , power coefficients  $\chi_P$ , and thermal conductivity  $\kappa$  obtained from Raman spectra.

The observed linear evolution of phonon frequencies in mono-layer MoS<sub>2</sub> can be attributed to the anharmonic vibrations of the lattice,[29] which mainly includes contributions from the lattice thermal expansion and the anharmonicity in phonon coupling. As the lattice expands or contracts due to temperature, the equilibrium position between vibrating atoms, and accordingly the inter-atomic forces change, induces shifts in the phonon.[36] Additionally, the lattice vibrational energies, governed by the Bose-Einstein distribution of thermal occupation, affect the inter-atomic

force energies, which further induce temperature-dependent variation of the phonon frequency. This linear behavior of Raman peak frequencies with temperature is seen in many materials, such as, graphene.[30, 31, 36]

In Table 3.1, the linear coefficients of suspended mono-layer MoS<sub>2</sub> suspended, few-layer MoS<sub>2</sub>, graphene, and graphite are summarized (this work is in bold). For comparison, similar measurements were performed on sapphire-supported mono-layer MoS<sub>2</sub> where no prominent difference in the first-order temperature coefficients for either mode was found. The small difference between  $\chi_T$  coefficients for the  $E_{2g}^1$  mode in suspended versus sapphire-supported likely results from varied in-plane strain applied by the substrate.[27]

The scattering rate of the phonons is related to the width of the phonon peak. The relationship between scattering rate and temperature for the two supported samples is shown in figure 3.3. The scattering rate increases as thermal energy is introduced into the material. The different samples, however, react to this energy with different increases in scattering rate. This may be attributed to the sample and substrate interacting with each other. The  $E_{2g}^1$  modes, or in plane modes, have an increase in scattering rate, but not as much as the  $A_{1g}$  or out of plane mode. This is because the out of plane mode is less constrained by the substrate as temperature increases. The supported sample with the overcoat of HfO<sub>2</sub>, in figure 3.3 is shown in squares, has a scattering rate that increases with a higher slope with increasing temperature than the supported sample without the overcoat, in circles.

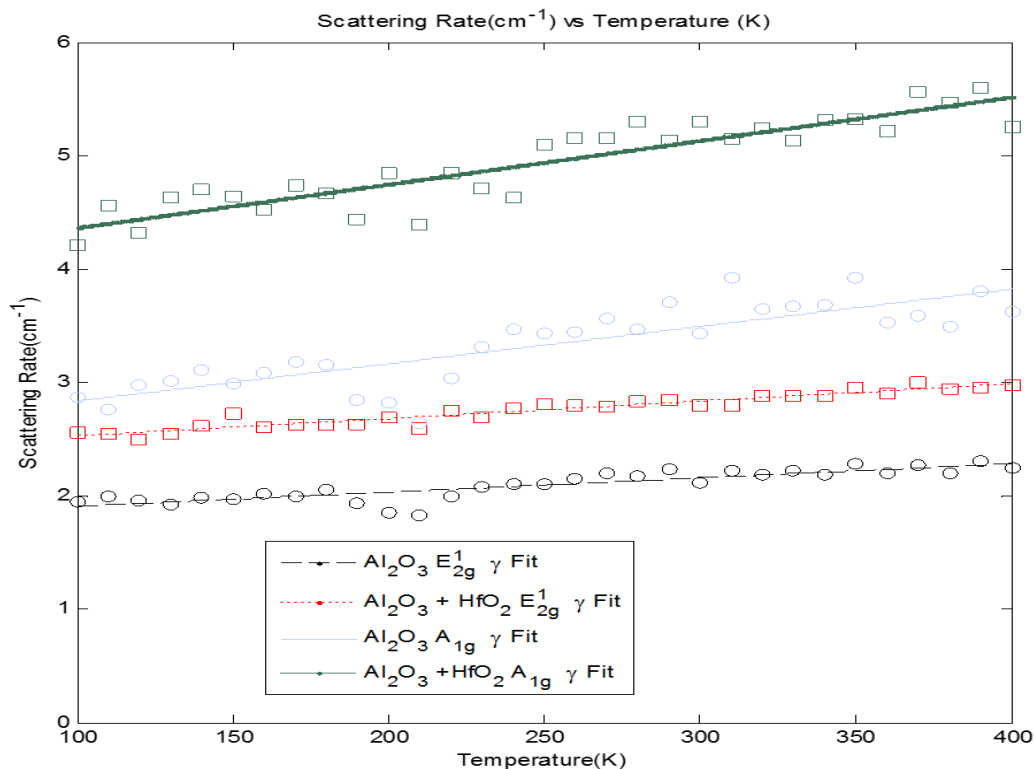


Figure 3.3: The scattering rate increases as thermal energy is introduced into the material. The different samples, however, react to this energy with different increases in scattering rate. This may be attributed to the sample and substrate interacting with each other.

## 3.2 Power Dependence

Strong thermal effects induced by the excitation laser power have been reported by others in the Raman spectra from substrate-supported MoS<sub>2</sub> flakes.[25, 28] Obviously the substrate plays a vital role in heat dissipation, therefore, the reported behavior is likely not intrinsic to MoS<sub>2</sub>. To obtain a comprehensive understanding of

the intrinsic optothermal MoS<sub>2</sub> properties, the laser power-dependent Raman spectra on a suspended flake was further studied. These Raman spectra are collected using a 488 nm solid-state laser for excitation with the beam focused by a 100X objective lens (NA = 0.9). The diffraction limited spot and estimated Gaussian beam width are approximately 0.67  $\mu\text{m}$  and 0.34  $\mu\text{m}$ , respectively. Four representative room-temperature Raman spectra collected at laser powers spanning from 0.075 mW to 0.309 mW are shown in figure 3.4(a). As the laser power increases, both of the Raman-active modes soften due to local heating of the mono-layer MoS<sub>2</sub>. To avoid damage to the sample, the excitation laser power was kept below 1 mW.

The Lorentzian-fit, Raman peak frequencies as a function of incident laser power are plotted in figure 3.4, where both the  $E_{2g}^1$  and  $A_{1g}$  modes soften linearly with increasing power. Beyond 0.3 mW of laser power, this thermal behavior saturates. The appearance of non-linear effects results either from the non-linearity of absorption or higher orders of the temperature-dependent coefficients. This can be seen in figure 3.5 where MoS<sub>2</sub> begins to saturate above 0.3 mW and the slope becomes less steep.

In figure 3.4(b), the low power-dependent peak positions are linear. In this low power range the frequency shift is given

$$\Delta\omega = \omega(P_2) - \omega(P_1) = \chi_P (P_2 - P_1) = \chi_P \Delta P \quad , \quad (3.3)$$

where  $\chi_P$ , the slope of power dependence in the linear region, is the first-order power dependent coefficient and  $P$  is the laser power. As with  $\chi_T$ , the fitted coefficients  $\chi_P$  for the  $E_{2g}^1$  and  $A_{1g}$  modes are very similar,  $-(12.8 \pm 0.2) \text{ cm}^{-1}/\text{mW}$  and  $-(10. \pm$

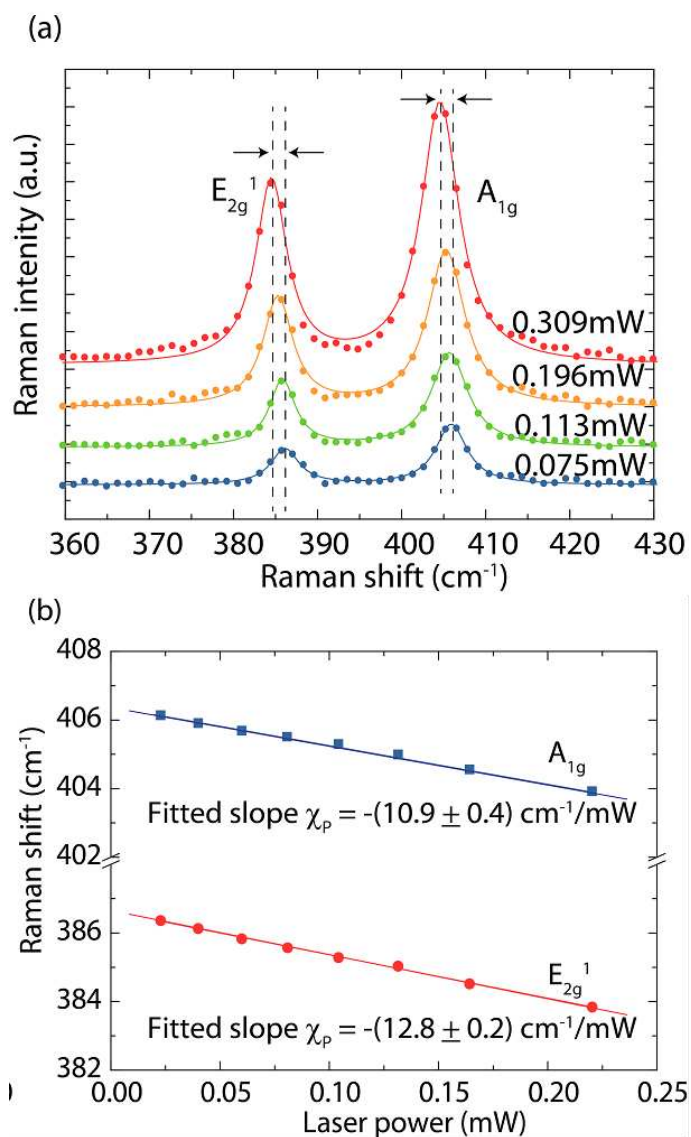


Figure 3.4: (a) Four example Raman spectra of suspended, single-layer, MoS<sub>2</sub> collected over increasing laser excitation power. The vertical offset is for display clarity. (b) Raman peak positions for both A<sub>1g</sub> (blue squares) and E<sub>2g</sub><sup>1</sup> (red circles) modes as a function of temperature. Fit lines and linear coefficients for temperature dependence,  $\chi_P$ , are shown.

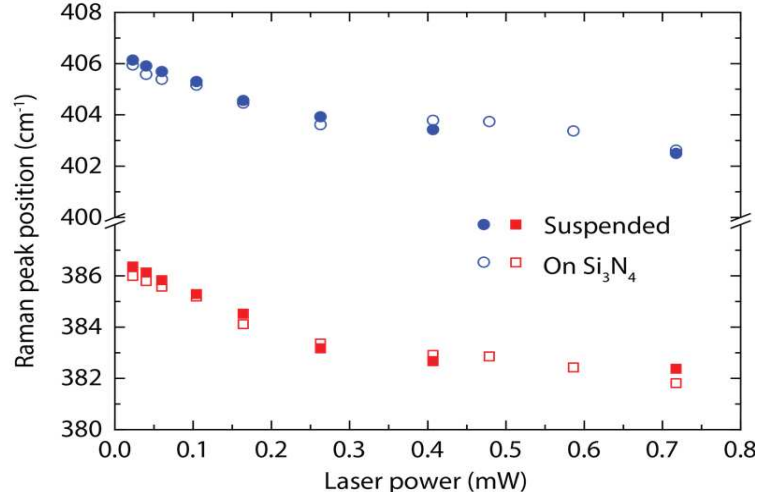


Figure 3.5: The non-linear power dependent peak frequency is shown. The peak position becomes non-linear above 0.3 mW

0.4)  $\text{cm}^{-1}/\text{mW}$ , respectively.[5] Note that these  $\chi_P$  values significantly exceed those reported[25] for substrate-supported mono-layer  $\text{MoS}_2$  and exceed by a factor of two those for suspended few-layer flakes.[34] Table 3.1 summarizes the laser power-coefficients for various  $\text{MoS}_2$  flakes.

For suspended mono-layer  $\text{MoS}_2$  both modes behave similarly in terms of the power-dependent slope, while for the substrate-supported mono-layer flake, the in-plane  $E_{2g}^1$  mode shows much smaller laser power dependence compared to the out-of-plane  $A_{1g}$  mode. The interaction is a strong manifestation of substrate-induced strain resulting from laser heating of the  $\text{MoS}_2$  while the substrate remains at room temperature (assuming negligible absorption of the laser). The strain is applied because the expansion of the  $\text{MoS}_2$  lattice is hindered by the cooler substrate. This point is further supported by a recent study on strain-dependent Raman spectra of

monolayer MoS<sub>2</sub> where only the  $E_{2g}^1$  mode is sensitive to the strain variation, but the  $A_{1g}$  mode does not respond.[27] This interaction between MoS<sub>2</sub> and the substrate has implications for electrical devices. As shown in table 3.1, the value for  $\kappa$  when the MoS<sub>2</sub> is suspended and single layer is lower than the few-layer MoS<sub>2</sub> and will be lower than the supported as well. These values for  $\kappa$  are extracted from experimental values  $\chi_T$  and  $\chi_P$ , which are different between mono-layer suspended and supported. The electronic device implications relate to the manufacturing process. If a device uses MoS<sub>2</sub> supported on a substrate, the substrate will change the value for  $\kappa$ .

### 3.3 Thermal Conductivity

The power dependence and temperature dependence of the Raman spectra was used to estimate the thermal conductivity  $\kappa$  of MoS<sub>2</sub> by comparing the peak shift for different temperatures and powers.  $\kappa$  is the property of a material that describes how well a material conducts heat. A high thermal conductivity means the material can dissipate heat quickly while a low thermal conductivity insulates heat. Thermal conductivity is

$$\kappa = \frac{A}{2\pi t} \frac{\partial P}{\partial T} \quad , \quad (3.4)$$

can be determined experimentally where  $t$  is the thickness,  $A$  is the absorbance. According to reference [4], absorbance equals 0.09 with an excitation laser of 514.8 nm. Experimentally this value was extracted by comparing the power and temperature dependent slopes along with other factors as shown in equation 3.4 Re-writing equa-

tion 3.4 in terms of phonon shift dependence

$$\kappa = \frac{A}{2\pi t} \frac{\partial\omega}{\partial P} \frac{\partial\omega}{\partial T} = \frac{A}{2\pi t} \frac{\frac{\partial\omega}{\partial T}}{\frac{\partial\omega}{\partial P}} \quad (3.5)$$

$$\kappa = \frac{A}{2\pi t} \frac{\chi_T}{\chi_P} \quad . \quad (3.6)$$

At this point the phonon dependence becomes evident,  $\frac{\partial\omega}{\partial T}$  is equal to the slope from figure 3.2,  $\chi_T$  and  $\frac{\partial\omega}{\partial P}$  is equal to the slope from figure 3.4,  $\chi_P$ . This gives the final thermal conductivity equation from experimental values shown in equation 3.6. The thermal conductivity of suspended mono-layer MoS<sub>2</sub> was found to be (34.5 ± 4) W m<sup>-1</sup> K<sup>-1</sup>.<sup>[5]</sup> This is lower than few layer MoS<sub>2</sub>, which can be seen with other thermal conductivities in table 3.2. The GaAs and MoS<sub>2</sub> have thermal conductivities that are considered to be a typical range for semiconductors, whereas Si has a higher thermal conductivity. This is why, when Si and graphene are compared, graphene has a very high thermal conductivity. This typical range for semiconductor's thermal

Material	$\kappa$ ( $\frac{W}{mK}$ )
MoS <sub>2</sub> Mono-layer <sup>a</sup>	34.5 ± 4
MoS <sub>2</sub> Few-layer <sup>b</sup>	52
Graphene Mono-layer <sup>c</sup>	5300 ± 480
Graphite <sup>d</sup>	2000
Silicon <sup>e</sup>	148
GaAs <sup>e</sup>	55

Table 3.2: <sup>a</sup> This work and ref [5], <sup>b</sup> ref [34] <sup>c</sup> ref [33], <sup>d</sup>ref [37], <sup>e</sup> ref [18]

conductivity does mean there will be barriers to overcome when trying to implement MoS<sub>2</sub> into electrical devices.

## Chapter 4

# Photoluminescence of Mono-layer

## MoS<sub>2</sub>

The photoluminescence (PL) of MoS<sub>2</sub> gives deep insight into the electronic band structure. MoS<sub>2</sub> in bulk form has an indirect band-gap around 1.2 eV. This band-gap slowly transitions to a direct band-gap around 1.8 eV as layers are removed from the bulk reaching mono-layer. This is a relatively large band-gap when compared to similar semiconductors like InSb, which can be used for electronic devices. This direct band-gap, as compared to other band-gaps in table 4.1 shows the transition between bulk and single-layer for MoS<sub>2</sub> along with other band-gaps of common materials including graphene, Si, and InSb. This existence of a direct band-gap is one of the many reasons single-layer MoS<sub>2</sub> has peaked the interests of electronic device developers. Graphene does not inherently have a direct or indirect band-gap. This existence of a direct band-gap in single-layer MoS<sub>2</sub> means it can be implemented in electronic devices as a semiconductor without augmentation to the band structure through strain, doping, or other mechanisms. The PL peak is an excitonic feature that, in single-layer MoS<sub>2</sub>, consists of more than a single transitions as discussed in

Crystal	Gap Type	Gap at Low T(eV)	Gap at 300 K (eV)
MoS <sub>2</sub> Single Layer <sup>c</sup>	Direct	1.89	1.87 ± 0.03
MoS <sub>2</sub> Bulk <sup>b</sup>	Indirect		1.2
Diamond <sup>a</sup>	Indirect	5.4	
Si <sup>a</sup>	Indirect	1.17	1.11
Ge <sup>a</sup>	Indirect	0.74	0.66
InSb <sup>a</sup>	Direct	0.23	0.17
GaAs <sup>a</sup>	Direct	1.54	1.43
Graphene <sup>b</sup>	NA	0	0

Table 4.1: <sup>a</sup> ref[18],<sup>b</sup> ref [9],<sup>c</sup> This work.

the previous section. These peaks have been identified as the neutral exciton, trion, and bound exciton. [4] The main excitonic feature consist of both the neutral exciton (A) and negative trion (A-), where they can, in more conducive environments, be separated and identified individually.[4] One way of separating the two peaks (A and A-) is by configuring the material into an electronic device, such as, a FET. Then a voltage bias either increase or reduce the amount of electrons in the system. With extra electrons, the A- trion peak becomes more prevalent, allowing for identification.[4] Another method shown to differentiate the two peaks is by lowering the temperature with liquid nitrogen or liquid helium.[4] This raises the energy that the A peak is luminescing at and lowers the energy of the A- peak.[4] These two methods are used to show that at room temperature and an unbiased configuration there are still two peaks in existence that make up the single excitonic feature. These two peaks need to be identified by their own fit parameters and must be allowed to move freely.

## 4.1 Temperature Dependence of Single-Layer MoS<sub>2</sub>

The temperature dependence of the PL Spectra is shown in figure 4.1 for several temperatures. We see several PL spectra of the suspended sample are over-laid to

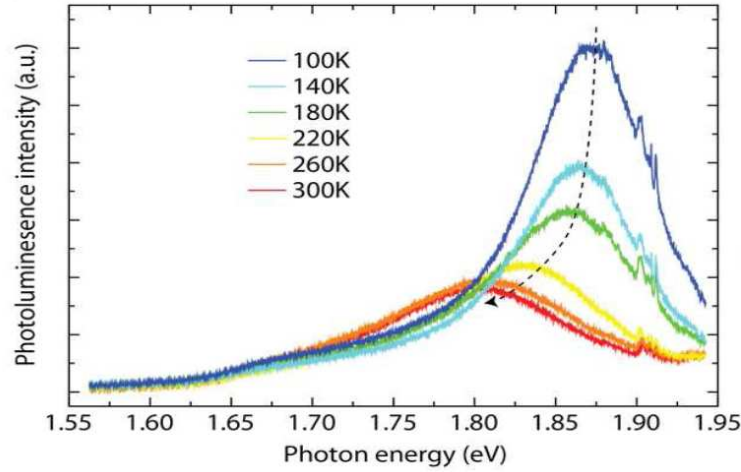


Figure 4.1: This shows six temperatures of PL spectra on the suspended sample.

show the general shape and position changes that the main excitonic peak undergo and the dashed line is a guide for the eye. The peak position red-shifts and broadens with temperature increase. Also there is a reduction in intensity of the luminescence as temperature increases. The temperature dependence is shown in figure 4.2(a) the suspended peak position (eV) from 100 K to 320 K and (b) shows the sapphire supported samples over a range of 100 K to 400 K. These were fitted with Gaussian curves defined by:

$$G(\omega) = \sum_i A_i e^{-\left(\frac{\omega - \mu_i}{\sigma_i}\right)^2}, \quad (4.1)$$

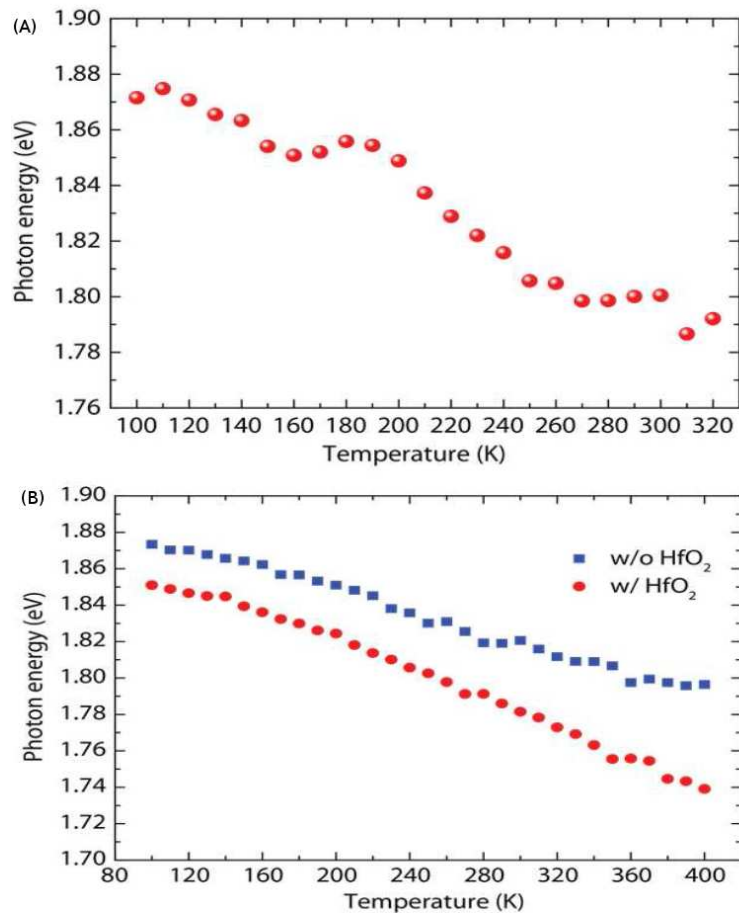


Figure 4.2: The temperature dependent peak positions are shown for three samples. (a) the peak position of the main excitonic structure, (b) Temperature dependent peak position of both samples on sapphire.

where there are three fitting parameters, all of which are indexed with  $i$  for multiple peaks. In the equation  $A$  represents the amplitude of the peak,  $\sigma$  represents the width of the peak given, and  $\mu$  represents the peak position. This temperature dependence shows that thermal energy changes the lattice or the band-structure. This is either intrinsic to the material's characteristics or caused by MoS<sub>2</sub> interacting with the substrate.

## 4.2 Power Dependence of Single-Layer MoS<sub>2</sub>

The power dependent study used the same experimental set-up for PL as described in chapter 2.4. The linear response shown in figure 4.3(a) between excitation power and PL emission intensity is only with excitation power from 6.18  $\mu$ W to 64  $\mu$ W. Above 64  $\mu$ W the PL response begins to exhibit a non-linearities. All three excitonic peaks show an increasing PL emission with increasing excitation power. The A- exciton, or trion, peak intensity has a linear coefficient of  $3.3 \times 10^4$  counts/mW, which is the steepest slope. The A exciton peak shows a linear coefficient of  $2.2 \times 10^4$  counts/mW and the defect peak shows a much more reduced slope of  $0.69 \times 10^4$  counts/mW. These slopes give insight into the nature of the peaks. The defect peak has a small slope because it is less related to a MoS<sub>2</sub> PL response and more so due to material or growth defects. As shown in figure 4.9(b) another linear response can be seen over the same power range. This linear response shows the relationship between excitation power and emitted energy through the photoluminescent process. The A exciton shows very little linear response to excitation power however the A-

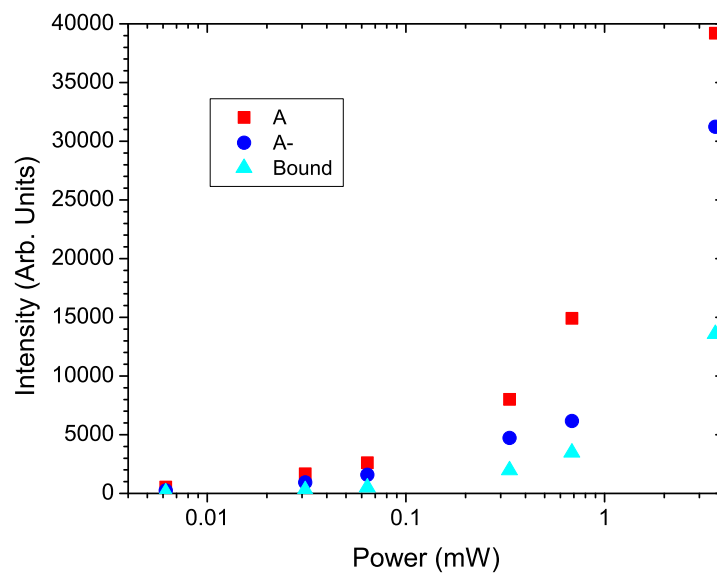


Figure 4.3: Power dependent PL peak amplitude. The peak amplitude's non-linear response of MoS<sub>2</sub> is shown for all three peaks; A peak in red, A- peak in blue, and the bound peak in cyan.

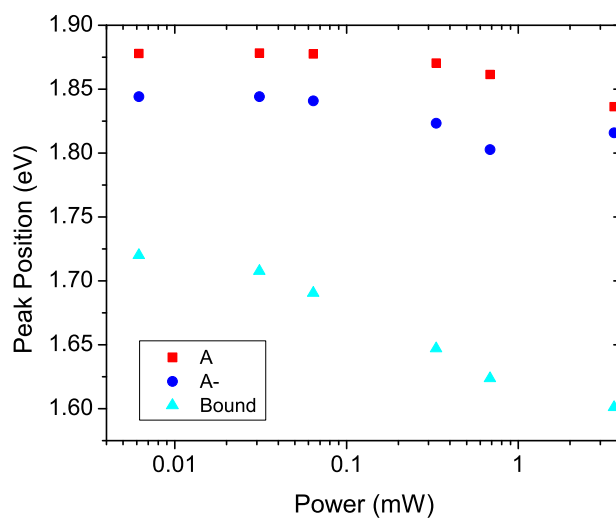


Figure 4.4: Power dependent PL peak position. The peak position's non-linear response of MoS<sub>2</sub> is shown for all three peaks; A peak in red, A- peak in blue, and the bound peak in cyan.

and defect peaks show a slight red-shift with increasing power. The A- exciton shifts with a slope of  $-0.091 \text{ eV/mW}$ , while the defect peak shifts with a more drastic slope of  $-0.24 \text{ eV/mW}$ . The excitation's peak width can relate to the broadness of emitted energy. A very broad PL peak relates to a wide range of energies being emitted from the peak's electron transitions. These responses are seen in Figure 4.5 (c). The A-

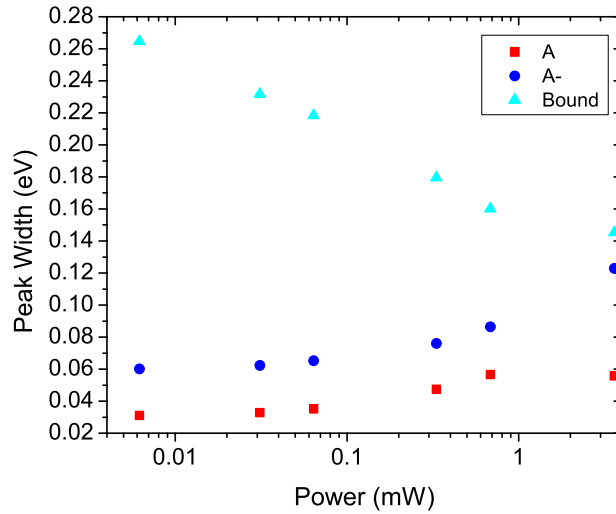


Figure 4.5: Power dependent PL peak width. The peak width's non-linear response of  $\text{MoS}_2$  is shown for all three peaks; A peak in red, A- peak in blue, and the bound peak in cyan.

peak shows a slope of  $.070 \text{ eV/mW}$ , while the A peak shows a more slight broadening slope of  $.036 \text{ eV/mW}$ . The defect peak shows a different linear response. The defect peak narrows with increasing power at a rate of  $-0.56 \text{ eV/mW}$ . All of these linear responses only work below an excitation power of  $0.06 \text{ mW}$ , anything above that power  $\text{MoS}_2$  begins to show signs of saturation.

Two spectra examples of the supported sample without  $\text{HfO}_2$  are seen in figures 4.6 and 4.7. There are three Gaussian curves, yellow is a fit for the defect peak,

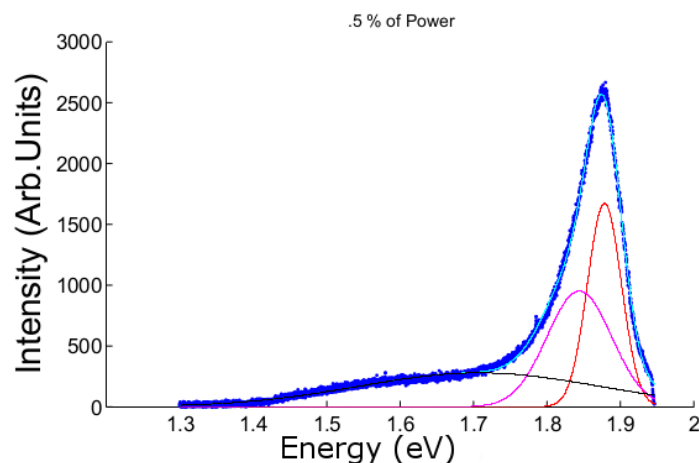


Figure 4.6: The spectrum data for the supported sample's PL power dependence at 0.0311 mW is shown fit with the (cyan) sum of the three Gaussian curves, (blue) the A exciton fit, (red) the A- exciton fit, and (black) the bound exciton fit

red is a fit for the A exciton, and magenta is a fit for the A- exciton. The fourth curve, black, is the sum of three Gaussian curves represented in equation 4.1. Figure 4.6 shows 0.031 mW, which is considered to be below the saturation point. Figure 4.7 represents 0.69 mW of power, which is above the saturation point. This drastic response for the intensities is in figure 4.3 shown in a semi-log scale. A positive response still holds true, increasing power still means increasing intensity, however, the rate of change for the intensity is lower above 0.06 mW. All three peaks show a decrease in the rate of change for the intensity. The peak position, or emitted photon energy, in figure 4.4 (semi-log scale), has a linearly decreasing slope. The non-linear response of the photon energy for all three peaks reaches a saturation

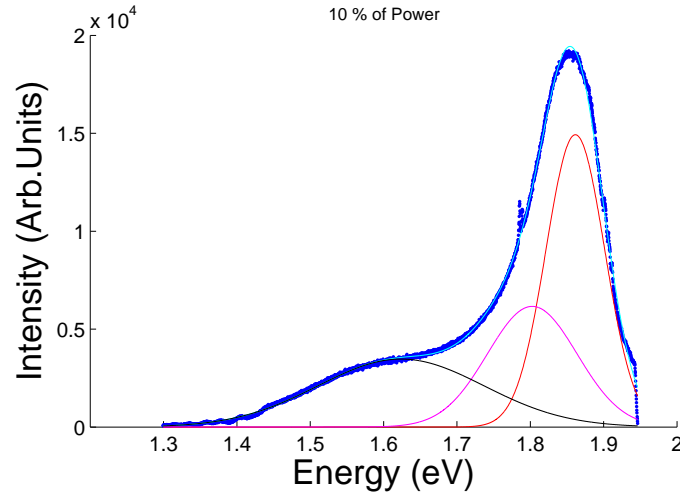


Figure 4.7: The spectrum data for the supported sample's PL power dependence at 0.685 mW is shown fit with the (cyan) sum of the three Gaussian curves, (blue) the A exciton fit, (red) the A- exciton fit, and (black) the bound exciton fit.

point. The width of these peaks or scattering rate, also becomes non-linear. This is in figure 4.5 shown in a semi-log scale. The A and A- peak linearly increase in energy width until it begins to saturate. The defect peak, however, is a decreasing energy width that begins to saturate instead of increasing. This simply means that the main excitonic peaks (A and A-) broaden, while the defect lower energy peak narrows with increasing input power.

Considering instead at the linear region of these PL spectra shows a similar relationship. Starting with the peak amplitude in figure 4.8 the red line is the linear fit where the red circle is the A exciton's fit parameter, the blue circle is the A- exciton's fit parameter, and the cyan circle is the bound exciton's fit parameter. We see the A, A- and bound peak amplitudes of MoS<sub>2</sub> increase linearly below 0.07 mW. The A peak has the greatest slope as well. The PL peak position of MoS<sub>2</sub> is also linear

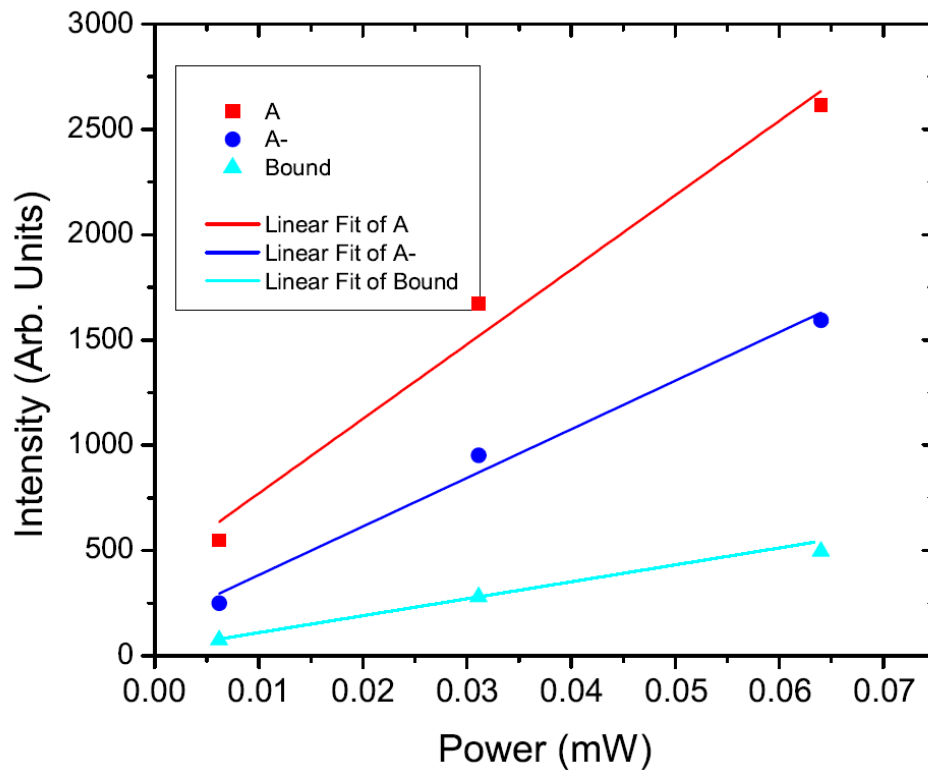


Figure 4.8: The photoluminescent power dependence of MoS<sub>2</sub> in the linear range is shown for amplitude. The red line is the linear fit where the red circle is the A exciton's fit parameter, the blue circle is the A- exciton's fit parameter, and the cyan circle is the bound exciton's fit parameter.

below 0.07 mW and is seen in figure 4.9. Once again, a similar trend is seen as before

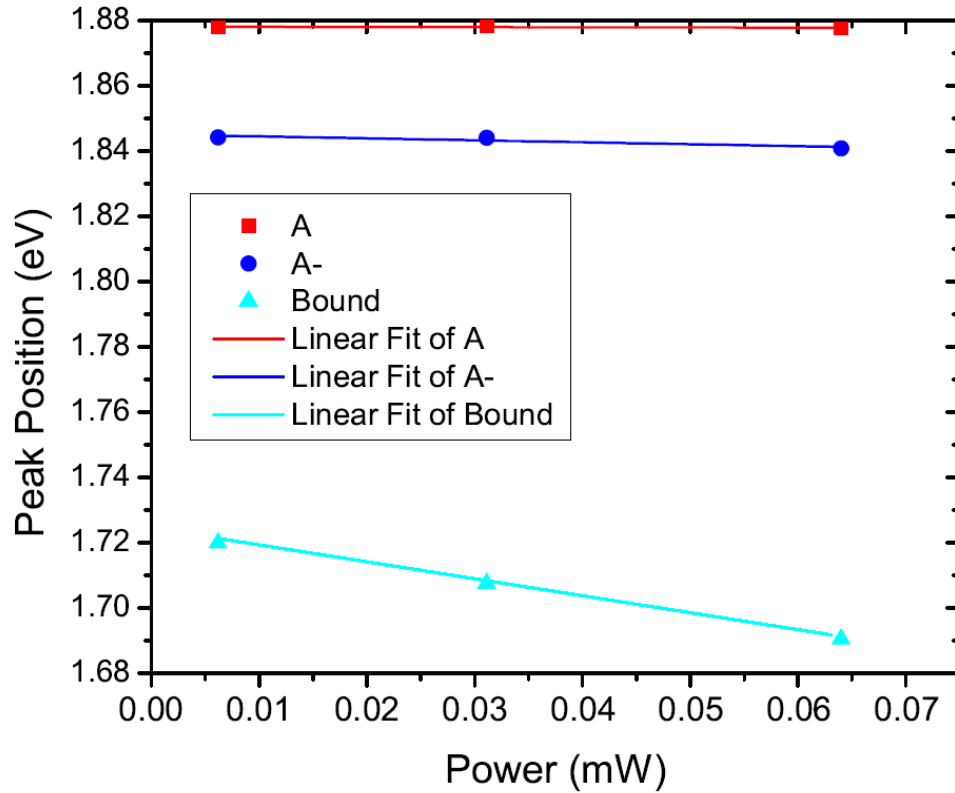


Figure 4.9: The photoluminescent power dependence of MoS<sub>2</sub> in the linear range is shown for peak position. The red line is the linear fit where the red circle is the A exciton's fit parameter, the blue circle is the A-, exciton's fit parameter, and the cyan circle is the bound exciton's fit parameter.

in the non-linear peak position. Here the A and A- peak positions both red-shift but only slightly where as the bound peak red-shifts at a greater rate. The peak width in the linear region does show an interesting trend. In figure 4.10 the peak width dependence of MoS<sub>2</sub> is seen for all three peaks. The A and A- peak both broaden but slightly with increasing power, however the bound peak narrows at a much more

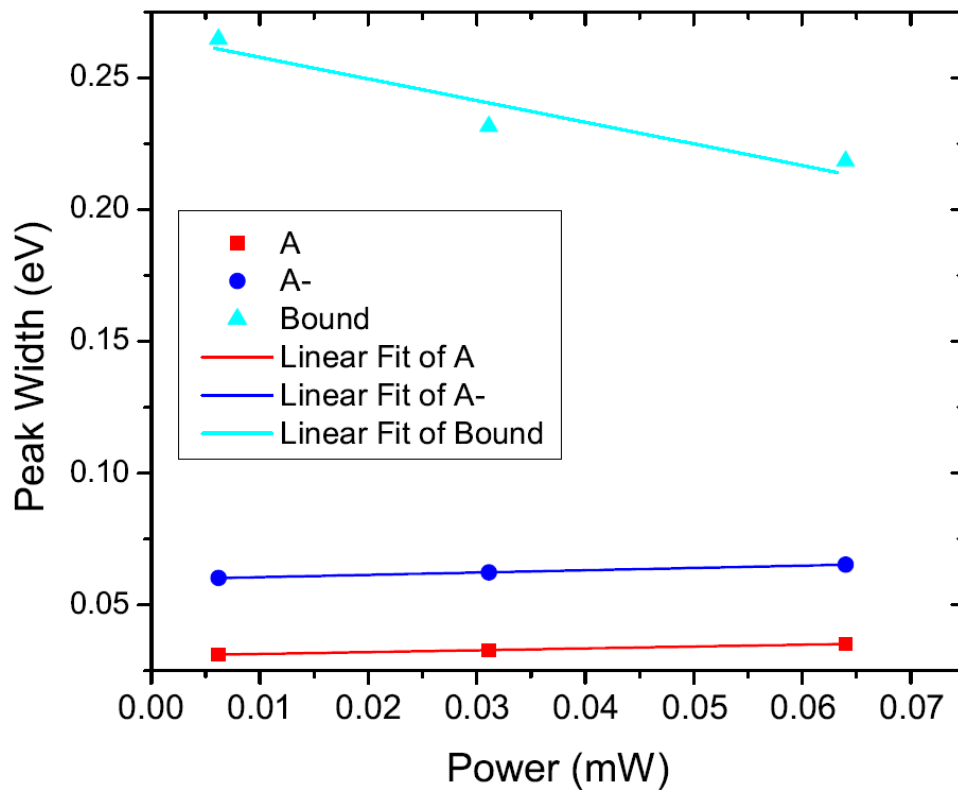


Figure 4.10: The photoluminescent power dependence of MoS<sub>2</sub> in the linear range is shown for peak width. The red line is the linear fit where the red circle is the A exciton's fit parameter, the blue circle is the A- exciton's fit parameter, and the cyan circle is the bound exciton's fit parameter.

drastic rate. This is the only parameter in the Gaussian fits that shows a different direction of shift between the three peaks.

The substrate also effects both Raman and PL as shown in table 4.2. The A exci-

Substrate	$A_{1g}$ Peak( $\text{cm}^{-1}$ )	$E_{2g}^1$ Peak ( $\text{cm}^{-1}$ )	A exciton(eV)
Suspended <sup>b</sup>	404.3	383.8	1.87
$\text{Al}_2\text{O}_3$ <sup>b</sup>	404.8	383.5	1.87
$\text{Al}_2\text{O}_3$ with $\text{HfO}_2$ <sup>b</sup>	402	383.7	1.85
$\text{SiO}_2$ <sup>a</sup>	404.4	385.2	1.85
$\text{Au}$ <sup>a</sup>	404.5	384.8	1.89
Gel-Film <sup>a</sup>	404.6	384.6	1.89
FLG <sup>a</sup>	405	385.2	1.89
Mica <sup>a</sup>	405.4	385.3	1.85
h-BN <sup>a</sup>	405.6	384.9	1.89

Table 4.2: This shows the pronounced effect a substrate has on both Raman and PL spectra for mono-layer  $\text{MoS}_2$ . <sup>a</sup> ref[38], <sup>b</sup> is the current work

ton location is interesting because the location represents the emitted photon energy, which is the direct band-gap at the K-point. This means the substrate changes the band structure through possible strain, or more likely via the dielectric environment. The lowest, or most red-shifted peak, is the sapphire-supported sample with the  $\text{HfO}_2$  overcoat. The suspended sample, with an A excitation of 1.87 eV, should be the closest to intrinsic  $\text{MoS}_2$  behavior because the probed material is suspended over holes. Thus, the suspended values reported here give a better understanding to the  $\text{MoS}_2$  band-gap than any of the other reported samples.

# Chapter 5

## Conclusion

Graphene, nearly a decade ago, spurred extensive research in the quickly developing field of condensed matter physics. This new research is focused on atomically thin, two-dimensional crystals such as single-layer transition-metal dichalcogenides (TMD) semiconductors and boron-nitride.[1, 2, 3, 6] Graphene shows characteristics that differ from bulk graphite that include low dimensionality, large thermal conductivity, and a band-gap when under strain. Graphene does not have a naturally occurring band-gap, it is a semi-metal where there is a high carrier mobility. Compared to graphene, the presence of a band-gap in TMDs is more desirable for electrical device applications, such as field-effect transistors (FETs). The incorporation of MoS<sub>2</sub> or other single layer materials like graphene allow manufacturers to approach a new size of electronics.[8] Recent experimental and theoretical work shows that these layered TMDs undergo a transition from indirect to direct band-gap when their thickness is reduced from bulk to mono-layer, leading to a pronounced photoluminescence.[9, 4, 10]

There are two main obstacles that must be broached before MoS<sub>2</sub> electronic devices have a chance. The thermal conductivity must be known and the band

structure's power and temperature dependence must be understood. Both of these topics were studied and proper physical models were applied.

Raman spectroscopy was used for thermal conductivity for both suspended and supported MoS<sub>2</sub> samples from 100 K to over 300 K. This was shown to be a negative slope for increasing temperature. Both the  $A_{1g}$  and  $E_{2g}^1$  peaks were observed and it was found for the suspended had a slope of  $-0.013 \text{ cm}^{-1}/\text{K}$  for  $A_{1g}$  and  $-0.011 \text{ cm}^{-1}/\text{K}$  for  $E_{2g}^1$ . The supported  $A_{1g}$  had a slope was  $-0.013 \text{ cm}^{-1}/\text{K}$  and  $E_{2g}^1$  had a slope of  $-0.017 \text{ cm}^{-1}/\text{K}$ .

The scattering rate for supported also differed between the  $A_{1g}$  and  $E_{2g}^1$ , where the  $A_{1g}$  scattering rate increased with temperature more drastically than the  $E_{2g}^1$  mode. This could be because the substrate is interacting with the out-of-plane mode more than the in plane mode. The thermal conductivity was extracted and is reported as  $(34.5 \pm 4) \text{ W m}^{-1} \text{ K}^{-1}$ . The PL is a powerful method to see the exciton dynamics along with values for the direct band-gap. When the electron radiatively recombines it emits photons with an energy related to the band-gap. The change of the peak position shows a change in band structure with temperature. The photon energy for suspended, supported with out HfO<sub>2</sub> and with HfO<sub>2</sub> all show a red-shift with increasing temperature but at different rates. The PL temperature dependent spectra show a decrease in amplitude, a lowering of photon energy, and a broadening with increasing temperature for the main,  $A$ , excitonic peak. The power dependence also showed a negative slope for the width and the photon energy, however the intensity increased with higher powers. The PL peaks are also highly dependent upon the substrate, the intensity, photon energy, and width all change with substrate. This

could change the way single layer MoS<sub>2</sub> is implemented in materials, possibly giving the electronic device components with specification like photon energy all fabricated with single-layer MoS<sub>2</sub> on various substrates.

Single-layer molybdenum disulphide research has began because of single layer material interest. Graphene started this interest and was found to have a very high thermal conductivity, which is useful for electronic devices, but is a semi-metal and has no natural band-gap. Single-layer MoS<sub>2</sub> naturally has a direct band-gap but has a thermal conductivity that is less than one one-hundredth of the thermal conductivity of graphene. The direct band-gap was measured using photoluminescent spectroscopy and found to be around 1.87 eV. The substrate also seems to change the band structure drastically with values that are  $\pm 0.05$  eV. The thermal conductivity was found using Raman spectroscopy and also showed the substrate works as a heat sink on the supported samples. With this new knowledge electronic devices can be created and possible sources of device failure can be addressed. These new single-layer materials have the potential to revolutionize the size of electronic devices in the near future making the understanding the physics of these new novel materials imperative.

# Bibliography

- [1] *Two-dimensional gas of massless Dirac fermions in graphene.*, K S Novoselov, A K Geim, S V Morozov, D Jiang, M I Katsnelson, I V Grigorieva, S V Dubonos, and A A Firsov, Nature **438(7065)** (2005).
  
- [2] *Two-dimensional atomic crystals.*, K S Novoselov, D Jiang, F Schedin, T J Booth, V V Khotkevich, S V Morozov, and A K Geim, Proc. Nat. Acad. Sci. USA **102(30)** (2005).
  
- [3] *The rise of graphene.*, A K Geim and K S Novoselov, Nat. Mater. **6(3)** (2007).
  
- [4] *Atomically Thin MoS<sub>2</sub>: A New Direct-Gap Semiconductor*, Kin Fai Mak, Changgu Lee, James Hone, Jie Shan, and Tony F. Heinz, Phys. Rev. Lett. **105(13)** (2010).
  
- [5] *Thermal Conductivity of Monolayer Molybdenum Disulfide Obtained from Temperature-Dependent Raman Spectroscopy*, Rusen Yan, Jeffrey R. Simpson, Simone Bertolazzi, Jacopo Brivio, Michael Watson, Xufei Wu, Andras Kis,

- Tengfei Luo, Angela R. Hight Walker, and Huili Grace Xing, ACS Nano (2013), doi:10.1021/nn405826k.
- [6] *Electronics and optoelectronics of two-dimensional transition metal dichalcogenides.*, Qing Hua Wang, Kouros Kalantar-Zadeh, Andras Kis, Jonathan N Coleman, and Michael S Strano, Nat. Nanotechnol. **7(11)** (2012).
- [7] *Energy gaps and a zero-field quantum Hall effect in graphene by strain engineering*, F Guinea, MI Katsnelson, and AK Geim, Nature Physics **6** (2009).
- [8] *Single-layer MoS<sub>2</sub> transistors.*, B Radisavljevic, A Radenovic, J Brivio, V Giacometti, and A Kis, Nat. Nanotechnol. **6(3)** (2011).
- [9] *Emerging photoluminescence in monolayer MoS<sub>2</sub>.*, Andrea Splendiani, Liang Sun, Yuanbo Zhang, Tianshu Li, Jonghwan Kim, Chi-Yung Chim, Giulia Galli, and Feng Wang, Nano Lett. **10(4)** (2010).
- [10] *Extraordinary Room-Temperature Photoluminescence in Triangular WS<sub>2</sub> Monolayers.*, Humberto R Gutiérrez, Nestor Perea-López, Ana Laura Elías, Ayse Berkdemir, Bei Wang, Ruitao Lv, Florentino López-Urías, Vincent H Crespi, Humberto Terrones, and Mauricio Terrones, Nano Lett. (2012).
- [11] *Phonons in single-layer and few-layer MoS<sub>2</sub> and WS<sub>2</sub>*, a. Molina-Sánchez and L. Wirtz, Physical Review B (**15**).
- [12] *High-mobility and low-power thin-film transistors based on multilayer MoS<sub>2</sub> crystals*, Sunkook Kim, Aniruddha Konar, Wan-Sik Hwang, Jong Hak Lee, Jiyoul

Lee, Jaehyun Yang, Changhoon Jung, Hyoungsub Kim, Ji-Beom Yoo, Jae-Young Choi, Yong Wan Jin, Sang Yoon Lee, Debdeep Jena, Woong Choi, and Kinam Kim, *Nat. Commun.* **3** (2012).

- [13] *Uniaxial strain on graphene: Raman spectroscopy study and band-gap opening*, Zhen Hua Ni, Ting Yu, Yun Hao Lu, Ying Ying Wang, Yuan Ping Feng, and Ze Xiang Shen, *ACS Nano* **2(11)** (2008).
- [14] *Valley polarization in MoS<sub>2</sub> monolayers by optical pumping*, Hualing Zeng, Jun-feng Dai, Wang Yao, Di Xiao, and Xiaodong Cui, *Nature nanotechnology* **7** (2012).
- [15] *Superior thermal conductivity of single-layer graphene.*, Alexander A Balandin, Suchismita Ghosh, Wenzhong Bao, Irene Calizo, Desalegne Teweldebrhan, Feng Miao, and Chun Ning Lau, *Nano Lett.* **8(3)** (2008).
- [16] *Anomalous Lattice Vibrations of Single- and Few-Layer MoS<sub>2</sub>*, Changgu Lee, Huguen Yan, Louis E Brus, Tony F Heinz, James Hone, and Sunmin Ryu, *ACS Nano* **4(5)** (2010).
- [17] *Thermal transport in suspended and supported monolayer graphene grown by chemical vapor deposition.*, Weiwei Cai, Arden L Moore, Yanwu Zhu, Xuesong Li, Shanshan Chen, Li Shi, and Rodney S Ruoff, *Nano Lett.* **10(5)** (2010).
- [18] *Introduction to Solid State Physics*, Charles Kittel (Wiley, 2005).
- [19] *Semiconductor Quantum Optics*, Mackillo Kira (Cambridge University Press, 2011).

- [20] *Graphene-based and graphene-like materials*, Alexander L Ivanovskii, Russ. Chem. Rev. **81(7)** (2012).
- [21] *Band-gap transition induced by interlayer van der Waals interaction in MoS<sub>2</sub>*, S. W. Han, Hyuksang Kwon, Seong Keun Kim, Sunmin Ryu, Won Seok Yun, D. H. Kim, J. H. Hwang, J.-S. Kang, J. Baik, H. J. Shin, and S. C. Hong, Phys. Rev. B **84(4)** (2011).
- [22] *Effects of confinement and environment on the electronic structure and exciton binding energy of MoS<sub>2</sub> from first principles*, Hannu-Pekka Komsa and Arkady V. Krasheninnikov, Phys. Rev. B **86(24)** (2012).
- [23] *Raman Spectrum of Graphene and Graphene Layers*, A. C. Ferrari, J. C. Meyer, V. Scardaci, C. Casiraghi, M. Lazzeri, F. Mauri, S. Piscanec, D. Jiang, K. S. Novoselov, S. Roth, and A. K. Geim, Phys. Rev. Lett. **97(18)** (2006).
- [24] *Identification of individual and few layers of WS<sub>2</sub> using Raman Spectroscopy.*, Ayse Berkdemir, Humberto R Gutiérrez, Andrés R Botello-Méndez, Néstor Perea-López, Ana Laura Elías, Chen-Ing Chia, Bei Wang, Vincent H Crespi, Florentino López-Urías, Jean-Christophe Charlier, Humberto Terrones, and Mauricio Terrones, Sci. Rep. **3** (2013).
- [25] *Raman and Photoluminescence Study of Dielectric and Thermal Effects on Atomically Thin MoS<sub>2</sub>*, Rusen Yan, Simone Bertolazzi, Jacopo Brivio, Tian Fang, Aniruddha Konar, A Glen Birdwell, N V Nguyen, Andras Kis, Debdeep Jena, and Huili Grace Xing arXiv:1211.4136 (2012).

- [26] *Symmetry-dependent phonon renormalization in monolayer MoS<sub>2</sub> transistor*, Biswanath Chakraborty, Achintya Bera, D. V. S. Muthu, Somnath Bhowmick, U. V. Waghmare, and A. K. Sood, Phys. Rev. B **(16)**.
- [27] *Raman Spectroscopy Study of Lattice Vibration and Crystallographic Orientation of Monolayer MoS<sub>2</sub> under Uniaxial Strain.*, Yanlong Wang, Chunxiao Cong, Caiyu Qiu, and Ting Yu, Small (2013), doi:10.1002/smll.201202876.
- [28] *Thermal effects on the characteristic Raman spectrum of molybdenum disulfide (MoS<sub>2</sub>) of varying thicknesses*, S. Najmaei, Z. Liu, P. M. Ajayan, and J. Lou, Appl. Phys. Lett. **100(1)** (2012).
- [29] *The lattice dynamics of an anharmonic crystal*, R.A. Cowley, Adv. Phys. **12(48)** (1963).
- [30] *Pressure dependence of infrared eigenfrequencies of KCl and KBr*, C Postmus, J R Ferraro, and S S Mitra, Phys. Rev. **174(3)** (1968).
- [31] *Temperature dependence of Raman scattering in silicon*, T R Hart, R L Aggarwal, and B Lax, Phys. Rev. B **1(2)** (1970).
- [32] *Temperature dependence of the first-order Raman phonon line of diamond*, Ming S. Liu, Les A. Bursill, S. Praver, and R. Beserman, Phys. Rev. B **61(5)** (2000).
- [33] *Temperature dependence of the Raman spectra of graphene and graphene multilayers.*, I Calizo, A A Balandin, W Bao, F Miao, and C N Lau, Nano Lett. **7(9)** (2007).

- [34] *Temperature-Dependent Raman Studies and Thermal Conductivity of Few-Layer MoS<sub>2</sub>*, Satyaprakash Sahoo, Anand P. S. Gaur, Majid Ahmadi, Maxime J.-F. Guinel, and Ram S. Katiyar, *J. Phys. Chem. C* **117(17)** (2013).
- [35] *The intrinsic temperature effect of the Raman spectra of graphite*, Ping Heng Tan, Yuan Ming Deng, Qian Zhao, and Wen Chao Cheng, *Appl. Phys. Lett.* **74(13)** (1999).
- [36] *Invited Article: Simultaneous mapping of temperature and stress in microdevices using micro-Raman spectroscopy.*, Thomas Beechem, Samuel Graham, Sean P Kearney, Leslie M Phinney, and Justin R Serrano, *Rev. Sci. Instrum.* **78(6)** (2007).
- [37] *Lattice thermal conductivity of graphene flakes: Comparison with bulk graphite*, DL Nika, S Ghosh, EP Pokatilov, and AA Balandin, *Applied Physics Letters* **94(20)** (2009).
- [38] *The effect of the substrate on the Raman and photoluminescence emission of atomically thin MoS<sub>2</sub>*, Michele Buscema, *ConMat*, arXiv (2013).

## Curriculum Vitae

Name: Michael Watson

Address: 6078 Watch Chain Way, Columbia, MD 21044

Program of Study: Applied Physics

Degree and Date to be Conferred: Master of Science, 2013

Secondary Education: Wilde Lake High School, Columbia, MD 2008

### COLLEGIATE INSTITUTIONS ATTENDED

Towson University ..... 2012-2013

Applied Physics M.S.

DePaul University ..... 2008-2012

Physics B.S. Minor: Math

### PROFESSIONAL PUBLICATIONS

[1] *EPICS Oscilloscope for Time-resolved Data Acquisition*, Williams G. Jackson, Michael A. Watson, Dohn A. Arms, Timothy M. Mooney, Donald A. Walko, and Eric C. Landahl, Nuclear Instruments and Methods in Physics Research Section A: Accelerators, Spectrometers, Detectors and Associated Equipment (2011).

[2] *Thermal Conductivity of Monolayer MoS<sub>2</sub> Obtained from Temperature-Dependent Raman Spectroscopy*, Rusen Yan, Jeffrey R. Simpson, Simone Bertolazzi, Jacopo Brivio, Michael Watson, Xufei Qu, Andras Kis, Tengfei Luo, Angela R. Hight Walker, Huili Xing ACS Nano (2013). doi:10.1021/nn405826k

